Article

Cheminformatics-Based Study Identifies Potential Ebola VP40 Inhibitors

Emmanuel Broni [1,2,3], Carolyn Ashley [3], Joseph Adams [2], Hammond Manu [1], Ebenezer Aikins [1], Mary Okom [1], Whelton A. Miller III [3,4,5,*], Michael D. Wilson [2,3] and Samuel K. Kwofie [1,6,*]

[1] Department of Biomedical Engineering, School of Engineering Sciences, College of Basic and Applied Sciences, University of Ghana, Legon, Accra LG 77, Ghana
[2] Department of Parasitology, Noguchi Memorial Institute for Medical Research (NMIMR), College of Health Sciences (CHS), University of Ghana, Legon, Accra LG 581, Ghana
[3] Department of Medicine, Loyola University Medical Center, Loyola University Chicago, Maywood, IL 60153, USA
[4] Department of Molecular Pharmacology and Neuroscience, Loyola University Medical Center, Maywood, IL 60153, USA
[5] Department of Chemical and Biomolecular Engineering, School of Engineering and Applied Science, University of Pennsylvania, Philadelphia, PA 19104, USA
[6] Department of Biochemistry, Cell and Molecular Biology, West African Centre for Cell Biology of Infectious Pathogens, College of Basic and Applied Sciences, University of Ghana, Accra LG 54, Ghana
* Correspondence: wmiller6@luc.edu (W.A.M.III); skkwofie@ug.edu.gh (S.K.K.);
Tel.: +1(708)-2168451 (W.A.M.III); +23-320-3797922 (S.K.K.)

Abstract: The Ebola virus (EBOV) is still highly infectious and causes severe hemorrhagic fevers in primates. However, there are no regulatorily approved drugs against the Ebola virus disease (EVD). The highly virulent and lethal nature of EVD highlights the need to develop therapeutic agents. Viral protein 40 kDa (VP40), the most abundantly expressed protein during infection, coordinates the assembly, budding, and release of viral particles into the host cell. It also regulates viral transcription and RNA replication. This study sought to identify small molecules that could potentially inhibit the VP40 protein by targeting the N-terminal domain using an in silico approach. The statistical quality of AutoDock Vina's capacity to discriminate between inhibitors and decoys was determined, and an area under the curve of the receiver operating characteristic (AUC-ROC) curve of 0.791 was obtained. A total of 29,519 natural-product-derived compounds from Chinese and African sources as well as 2738 approved drugs were successfully screened against VP40. Using a threshold of −8 kcal/mol, a total of 7, 11, 163, and 30 compounds from the AfroDb, Northern African Natural Products Database (NANPDB), traditional Chinese medicine (TCM), and approved drugs libraries, respectively, were obtained after molecular docking. A biological activity prediction of the lead compounds suggested their potential antiviral properties. In addition, random-forest- and support-vector-machine-based algorithms predicted the compounds to be anti-Ebola with IC_{50} values in the micromolar range (less than 25 μM). A total of 42 natural-product-derived compounds were identified as potential EBOV inhibitors with desirable ADMET profiles, comprising 1, 2, and 39 compounds from NANPDB (2-hydroxyseneganolide), AfroDb (ZINC000034518176 and ZINC000095485942), and TCM, respectively. A total of 23 approved drugs, including doramectin, glecaprevir, velpatasvir, ledipasvir, avermectin B1, nafarelin acetate, danoprevir, eltrombopag, lanatoside C, and glycyrrhizin, among others, were also predicted to have potential anti-EBOV activity and can be further explored so that they may be repurposed for EVD treatment. Molecular dynamics simulations coupled with molecular mechanics Poisson–Boltzmann surface area calculations corroborated the stability and good binding affinities of the complexes (−46.97 to −118.9 kJ/mol). The potential lead compounds may have the potential to be developed as anti-EBOV drugs after experimental testing.

Keywords: Ebola virus; VP40; anti-Ebola; natural products; molecular docking; molecular dynamics simulations; ADMET; MM/PBSA

1. Introduction

Ebola virus disease (EVD) is a severely fatal disease caused by the virulent Ebola virus (EBOV). As a zoonotic infection with its putative reservoir as fruit bats [1], it has been shown that Ebola can be transmitted from animals to humans through natural means; transmission of the virus is also plausible via proximate contact with the body fluids or skin abrasions of infected people. EBOV found in semen is now a major concern as the virus can be sexually transmitted even after about 7 months from the day of recovery [2–6]. In general, patients infected with EVD have a predictable clinical course; thus, the early stages of the infection manifest symptoms that are considered a non-specific febrile illness, while progressing to severe gastrointestinal symptoms and severe hemorrhagic fever after weeks of infection and, subsequently, causing lethality with an up to ~90% fatality rate (with an average of about 50%) [7,8]. The virulence and lethality of this virus are due to diverse factors, particularly its ability to replicate and the assembly and budding of new virus particles at the early stages of the infection. Ebola virus is classified under the *Filoviridae* family of enveloped, single-stranded, negative-sense RNA viruses [9]. The virus forms a thread-like shape with a uniform diameter of ~80 nm and a typical length between 600 nm and 1400 nm [8,10,11].

The 2013–2016 outbreak was the largest in history, resulting in approximately 28,000 cases and 11,000 deaths [12,13]. More recently, there were EVD outbreaks in the Democratic Republic of Congo and Guinea in 2021 and Uganda in 2022. The highly virulent and lethal nature of EBOV highlights the need to develop therapeutic agents that limit the pathogenesis and spread of the virus. The genome of EBOV contains seven genes that encode seven different structural viral proteins (VP): glycoprotein (GP), nucleoprotein (NP), VP30, VP40, VP24, VP35, and RNA-dependent RNA polymerase (RdRp) [14]. Each structural protein plays a role in the lifecycle of the virus. The major matrix protein and the most extensively expressed protein, VP40, is a 326-amino acid protein that regulates viral assembly, budding, and egress and participates in transcription and viral replication through host cell RNA metabolism [15]. The X-ray structure of the VP40 protein revealed a matrix protein structure with an N-terminal domain (NTD) that is essential for oligomerization and a C- terminal shown to be essential in membrane binding through interactions with both host and cellular components [16,17].

The expression of only VP40 in mammalian cells is enough to assemble and form virus-like particles (VLPs) that are similar in size and shape to the parent virus [18]. VP40 has also been shown to regulate viral transcription, which represents a structural target in the lifecycle of the virus [19]. Crystallographic studies have shown that VP40 has two distinct domains within its structure: the NTD and the C-terminal domain (CTD) [19]. NTD interactions are responsible for VP40 dimer formation in the cytoplasm. Multiple dimers join to undergo oligomerization and form a perinuclear ring, while CTD interactions are responsible for plasma membrane binding and the coordination of higher-order oligomerization [16]. The NTD and CTD seem loosely connected, and at the NTD, the formation of ring structures (known as octameric rings) occurs where each of the eight NTD subunits can bind an RNA trinucleotide [15].

The role of the octameric ring has been identified to regulate viral transcription and replication in infected cells [19]. The crystal structure of VP40 corresponds to that of an octamer, which forms a pore-like structure and binds to RNA. The crystallographic structure of VP40 RNA shows that the Arg134 and Phe125 of VP40 mainly interact with RNA [20], and this interaction plays a critical role in octamer formation and promotes the replication of the Ebola virus.

Currently, there are two FDA-approved treatment methods for EVD. The first, REGN-EB3 (Inmazeb), is a mixture of three monoclonal antibodies that target the glycoprotein of the virus and block the attachment and entry of the virus [21–23]. The second, Ansuvimab (Ebanga), also prevents the virus from entering host cells, thereby limiting viral replication [24,25]. Though small molecules have been shown to have a logistical advantage over antibody therapy [26], EVD patients are limited to the use of these antibody therapies [27].

Other treatment options include supportive and symptomatic therapies, which are employed to treat the clinical symptoms of the disease [28,29]. A disproportionate number of the most advanced therapeutics currently under evaluation are small molecules directed against the RdRp required for viral replication. These include BCX4430 [30,31], favipiravir (T-705) [32], and small-interfering RNA (siRNA), the last of which suppresses viral RNA levels by degrading mRNA transcripts that interfere with translation [33].

Natural products exhibit distinctive and interesting characteristics or properties including structural and chemical diversity, thereby giving them a wider range of bioactivities. These unique properties of natural products grant them special advantages suitable for investigations regarding the discovery of new therapeutics against most infections, for which EVD is not an exception [34]. Apparently, most recent studies have emphasized the acquisition of drugs from synthetic products while being fairly neglectful of natural products. Therefore, there is a need to identify natural lead compounds from these underexploited sources that can effectively inhibit the activities of VP40 within the lifecycle of EBOV.

Following the successes of the application of computer-aided drug design (CADD) strategies to drug development processes, this study sought to virtually screen natural-product-derived compounds that target the VP40 protein and investigate the antiviral mechanisms of action of potential lead compounds. The study further profiled the potential lead compounds to test absorption, distribution, metabolism, excretion, and toxicity (ADMET). CADD approaches play key roles in drug discovery; therefore, efficient molecular docking and molecular dynamics (MD) simulations coupled with ADMET characterization will help identify potential Ebola VP40 inhibitors.

2. Results and Discussion

2.1. Protein Extraction and Preparation

A search for experimentally determined 3D structures of the EBOV VP40 protein via the Protein Data Bank (RCSB PDB) [35–37] revealed 13 structures. However, all 13 experimentally solved VP40 structures had numerous missing residues. For example, the structure of 1H2C, which was solved at a good resolution of 1.60 Å [20], and the structure of 7K5L, which was solved at an even better resolution of 1.38 Å [38], were both missing residues 1–68 in their NTDs. By visualizing the structures via PyMOL, it was observed that the missing residues were very close to the RNA binding site and the loop region; thus, they could not be ignored since they could influence ligand binding and may be involved in VP40–ligand interactions.

2.1.1. Structure Remodeling

The amino acid sequence of the VP40 NTD extracted from UniprotKB was used to remodel the protein using Modeller and I-TASSER in order to predict a reasonable VP40 structure. A previous study used UCSF Chimera to fix the missing residues on the structure of 3TCQ prior to molecular docking [39]. Modeller generated five models using the 3D structures of 3TCQ and 7K5L as templates. All five models had a very good genetic algorithm 341 (GA341) score of 1 and DOPE scores of -1.743×10^4, -1.780×10^4, -1.736×10^4, -1.741×10^4, and -1.756×10^4, respectively. However, the folding of the missing residues was not fixed in all five Modeller-generated structures. I-TASSER generated five models of the VP40 protein's NTD with C-scores of -0.68, -1.90, -2.93, -2.73, and -1.63. The C-score determines the confidence of the structure and ranges from -5 to 2, where a higher value signifies a model with a higher confidence value and vice versa [40–42]. I-TASSER used a crystal structure of the VP40 with PDB ID 1ES6 as the parent template for modelling. 1ES6's structure was experimentally determined via X-ray with a resolution of 2 Å; consequently, it was determined that only residues 1 to 43 are missing in its NTD [43]. The missing residues of all five I-TASSER structures were more reasonably folded compared to those from Modeller. Thus, the best I-TASSER model (with a C-score of -0.68 and an estimated TM-score of 0.63 ± 0.14) was selected as the most reasonable structure of VP40's

NTD (Figure 1). Aligning the selected structure to the structures of 1ES6, 7K5L, and 1H2C produced RMSD values of 0.332, 2.083, and 2.069 Å, respectively. These RMSD values are acceptable, as RMSD values below 2.5 Å are considered reasonable [44].
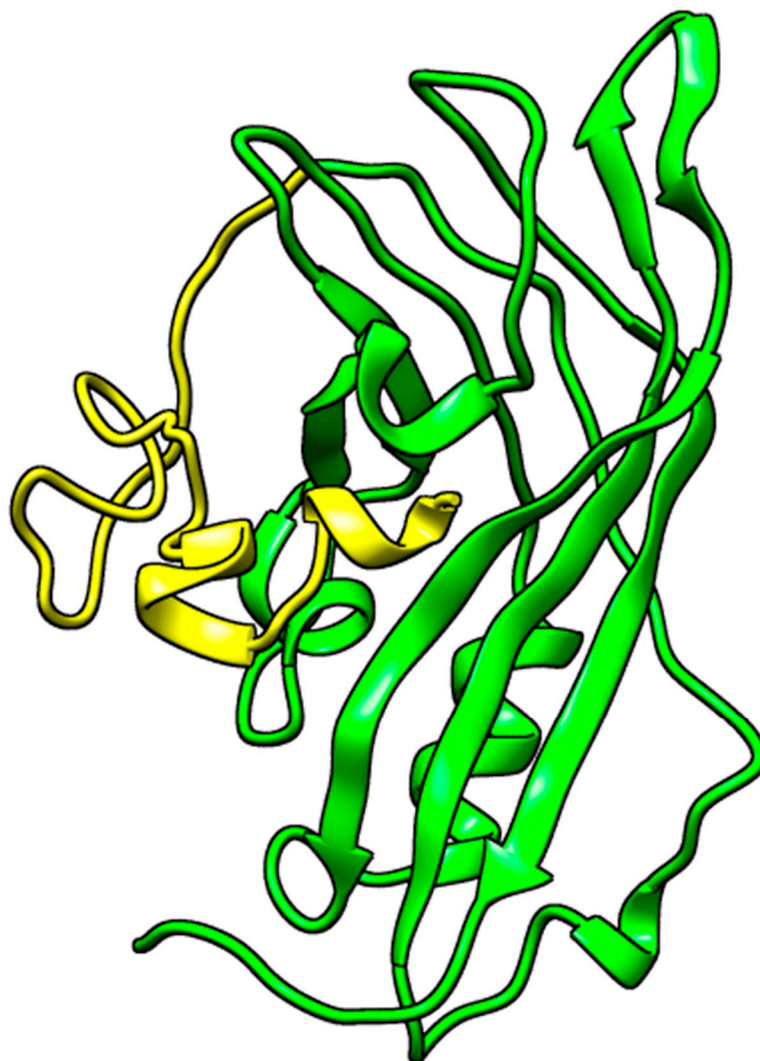
Figure 1. Structure of the selected VP40 NTD model generated via I-TASSER using 1ES6's structure as template. Image was generated using UCSF Chimera version 1.16 [45]. Regions colored yellow represent missing residues that were remodeled.

2.1.2. Energy Minimization of Structure

The selected structure was then energy-minimized using OPLS and CHARMM36 force fields with the intent of selecting the structure with the least energy. The OPLS force field achieved the lowest energy state with -8.09×10^5 kJ/mol after 845 ps (in 846 steps) while the structure with the CHARMM force field reached -7.874×10^5 kJ/mol after 706 ps (in 707 steps) (Figure S1). Thus, the structure that was minimized using the OPLS force field was selected for this study.

2.2. Binding Site Determination

The residues Thr123, Phe125, and Arg134 of VP40 have been reported to interact with RNA [20]. Mutations of residues Lys127, Thr129, and Asn130 in the loop region of the NTD of VP40 were shown to reduce the plasma membrane localization of EBOV VP40. The mutation of these residues also significantly reduces VP40 oligomerization and limits the release of VLPs [46]. Interaction maps from previous studies show that these residues overlap with the RNA binding site [39,47]. CASTp also predicted 31 binding

cavities; however, all 30 except the binding site on the loop region were relatively too small such that no compound could fit or dock into them. The binding site was predicted to have an area and volume of 303.2 Å^2 and 438.3 Å^3, respectively. The binding site residues consisted of Leu6, Pro7, Pro10, Met14, Ala27, Arg28, Asn31, Ser32, Asn33, Gly99, Val100, Ala101, Asp102, Lys104, Thr105, Asp144, His145, Pro146, Leu147, Arg148, Arg151, Trp191, Thr192, and Asp193. This binding site is consistent with that predicted previously using Site Finder [48]. The study also suggested that there is a higher likelihood for a small molecule to bind in this region [48].

The residues 7PTAP10 and 10PPEY13 (overlapping late (L)-budding domains: 7PTAPPEY13 in EBOV) have been experimentally shown to interact with host cellular WW-domain-bearing proteins, including neural-precursor-cell-expressed developmentally down-regulated protein 4 (Nedd4), tumor susceptibility gene 101 (Tsg101), AIP1/Alix, and HECT domain E3 ubiquitin protein ligase 1 (HECTD1), among others [49–51]. These interactions regulate the budding and egress of Ebola-virus-like particles (VLPs) from host cells [50,51]. Another study also showed that small molecule probes that target the PPxY domain inhibit the egress of a broad range of RNA viruses [52,53]. Trp191 stabilizes hydrophobic interactions in VP40, thus providing flexibility for the loop region to interact with lipids [54]. In vitro studies have reported that interfering with local Trp191 interactions induced dimer instability [54]. The binding site on the loop region predicted via CASTp contains these residues, thereby rendering the site a reliable target. Thus, the RNA binding site and the binding pocket predicted via CASTp (on the loop region) were considered for the molecular docking studies.

2.3. Validation of Docking Protocol

The ability of a docking tool to differentiate between potential binders (or inhibitors) and decoys is very important in the computational drug discovery pipeline [55,56]. AutoDock Vina was predicted to have AUC and BEDROC ($\alpha = 20$) values of 0.791 (Figure 2) and 0.442, respectively. In addition, the TG and RIE values of AutoDock Vina were determined to be 0.536 and 7.315, respectively. AUC values usually range from 0 to 1, with a value of 1 implying a perfect degree of classification between actives and decoys. AUC values within the 0.5 to 0.7 range are considered to provide moderate distinctive ability, while values below 0.5 imply poor discrimination ability between active and decoys [57,58]. However, a molecular docking method with an AUC above 0.5 and a TG above 0.4 is considered good performance and is reproducible under similar experimental conditions [59]. The results presented herein show that AutoDock Vina performed very well and can reasonably distinguish between VP40 actives and inactives.

2.4. Molecular Docking Studies

The AfroDb, NANPDB, and TCM libraries were obtained and virtually screened against VP40 to shortlist compounds with reasonably good docking scores. The docking results were ranked according to docking scores in a decreasing order. A docking score threshold of −8 kcal/mol and lower was used to filter the top compounds from the AfroDb, NANPDB, TCM, and Approved compounds libraries since nilotinib (a known inhibitor with the best docking score) had a docking score of −7.9 kcal/mol.

For the AfroDb library, 773 compounds were successfully screened against the VP40 protein. Only 7 AfroDb compounds had docking scores of −8 kcal/mol and below. The lowest docking score was observed for ZINC000095486217 with a score of −8.6 kcal/mol, while ZINC000028462577 had a score of −8.3 kcal/mol. The compounds ZINC000034518176 and ZINC000095485942 both had a docking score of −8.1 kcal/mol (Table 1), while ZINC000014825190, ZINC000085594516, and ZINC000095486263 all had a docking score of −8 kcal/mol.
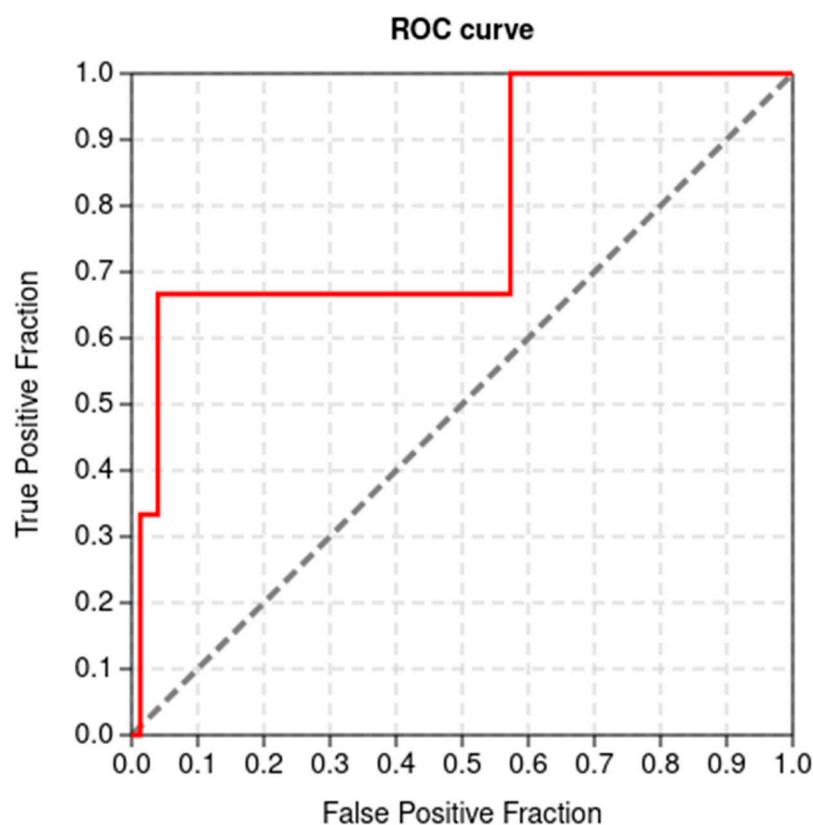
Figure 2. ROC curve generated using 150 decoys and 3 known inhibitors of EBOV VP40 to assess molecular docking performance. An AUC ROC value of 0.791 was obtained.

Table 1. Docking scores and interacting residues of some top compounds that were docked into VP40's NTD.

Compound	Source/Library	Docking Score	Hydrogen Bonds (Bond Length (Å))	Hydrophobic Contacts
ZINC000034518176	AfroDb	−8.1	Gly139 (3.05)	Phe36, Asn43, Pro47, Thr121, Phe125, Arg134, Asn136, Arg137, and Leu138.
ZINC000095485942	AfroDb	−8.1	Thr129 (2.72) and Asn130 (2.85, 3.25)	Pro131, Gln159, Glu160, Pro165, Val166, Pro169, and Gln170.
NANPDB2933	NANPDB	−8.5	Val166 (3.23) and Gln167 (3.09, 3.26).	Ala128, Thr129, Pro131, Gln159, Glu160, Pro165, and Gln170.
ZINC000085531689	TCM	−8.9	Asn130 (2.99, 3.05), Gln159 (2.94, 3.22), and Pro169 (2.71).	Glu160, Gln167, Leu168, Gln170, and Phe172.
ZINC000014089759	TCM	−8.8	Arg21 (3.02, 3.03), Pro39 (3.1), and Lys127 (3.04).	Tyr13, Tyr18, Pro19, and Asn23.
ZINC000085545967	TCM	−8.8	Gln159 (3.16), Leu168 (3.14), and Leu169 (3.16).	Lys127, Ala128, Thr129, Pro131, Glu160, Pro165, Val166, Gln167, Gln170, and Phe172.
ZINC000085568136	TCM	−8.7	Asp45 (3.11) and Gly84 (3.13).	Val42, Gly44, Gly126, Lys127, Als128, Tyr171, and Thr173.
ZINC000095912717	TCM	−8.7	Gln159 (3.09), Val166 (3.14), and Gln170 (3.04).	Ala128, Asn130, Pro131, Glu160, Pro164, Pro165, Gln167, Leu168, and Pro169.
ZINC000014089743	TCM	−8.6	Arg21 (2.96), Ser24 (2.97), and Pro39 (3.09).	Tyr13, Tyr18, Pro19, Asn23, and Lys127.
ZINC000101564200	TCM	−8.6	Val166 (2.78, 3.09), Pro169 (2.77), and Gln170 (3.09).	Lys127, Ala128, Thr129, Pro131, Gln159, Glu160, Pro165, Gln167, and Leu168.
ZINC000085504890	TCM	−8.5	Asn130 (3.23) and Gln170 (3.16)	Lys127, Ala128, Thr129, Pro131, Gln159, Glu160, Pro165, Val166, Gln167, Leu168, and Pro169.
ZINC000095909661	TCM	−8.5	Asn130 (2.8) and Pro169 (3.18)	Ala128, Thr129, Pro131, Gln159, Glu160, Leu168, and Gln170.
ZINC000070454124	TCM	−8.4	Val42 (3.05) and Thr129 (3.19).	Val20, Arg21, Pro39, Asn43, Gly44, Lys127, Ala128, Leu132, and Tyr171.

Table 1. *Cont.*

Compound	Source/Library	Docking Score	Hydrogen Bonds (Bond Length (Å))	Hydrophobic Contacts
Doramectin	Approved	−9.1	Glu12 (2.72), Asn130 (3.14), Gln159 (2.8), Leu168 (3.33), and Pro169 (3.06).	Tyr13, Lys127, Ala128, Thr129, Pro131, Glu160, Phe161, Pro165, and Gln170.
Ledipasvir	Approved	−9	-	Arg21, Pro39, Val42, Asn43, Gly44, Asp45, Thr46, Ser83, Gly84, Lys127, Ala128, Thr129, and Tyr171.
Avermectin B1 (Abamectin)	Approved	−8.7	Glu12 (2.89), Asn130 (3.04), Gln159 (2.85), and Leu168 (3.11).	Thr8, Tyr13, Ala128, Thr129, Pro131, Glu160, Phe161, Pro165, Pro169, Gln170, and Phe172.
Elbasvir	Approved	−8.7	Asp45 (3.16)	Arg21, Pro39, Val42, Asn43, Gly44, Thr46, Ser48, Gly84, Lys127, Ala128, Thr129, Tyr171, Thr173, Phe174, and Asp175.
Venetoclax (ABT-199, GDC-0199)	Approved	−8.5	Gly44 (3.16), Thr46 (2.88), Gly84 (3.07), and Thr173 (2.85).	Ser48, Asn49, Ile82, Ser83, Leu168, Pro169, Gln170, Tyr171, and Asp175.
Revefenacin	Approved	−8.5	Asp45 (2.9) and Lys127 (2.8)	Tyr18, Val20, Arg21, Pro39, Val42, Gly44, Ser83, Ala128, Thr129, Tyr171, and Phe172.
Glecaprevir	Approved	−8.4	Asn130 (2.93), Gln159 (2.99), Val166 (2.8), and Leu168 (3.31).	Ala128, Thr129, Glu160, Phe161, Pro165, Gln167, Pro169, and Gln170.
Nilotinib	Inhibitor	−7.9	-	Tyr18, Arg21, Pro39, Val42, Gly44, Gly126, Lys127, Ala128, Thr129.
Imatinib	Inhibitor	−7.6	-	Pro39, Glu40, Ser41, Val42, Gly44, Asp45, Ser83, Gly84, Gly126, Lys127, and Tyr171.
Cepharanthine	Inhibitor	−7.3	-	Asn130, Pro131, Gln159, Glu160, Pro165, Val166, Gln167, and Leu168.
Sangivamycin	Inhibitor	−6.3	Pro169 (3.03, 3.2) and Val166 (2.82, 3.11).	Ala128, Thr129, Pro131, Gln159, Glu160, Pro165, Leu168, Gln170, and Phe172.

For the NANPDB library, a total of 3615 compounds were successfully screened against the VP40 protein. A total of 11 compounds were observed to have docking scores of −8 kcal/mol and below. The compound NANPDB4060 demonstrated the lowest docking score with respect to VP40 with a value of −8.8 kcal/mol, followed by NANPDB2933 (Table 1) and NANPDB4059 with docking scores of −8.5 and −8.4 kcal/mol, respectively. NANPDB322, NANPDB362, NANPDB4055, and NANPDB5641 all had docking scores of −8.1 kcal/mol, while NANPDB4057, NANPDB4240, NANPDB552, and NANPDB6298 all had a docking score of −8 kcal/mol.

For the TCM library, a total of 25,131 compounds were successfully screened against VP40. The docking scores of all 25,131 compounds in the TCM library ranged from −1.4 to −9 kcal/mol. A total of 163 compounds were observed to have docking scores of −8 kcal/mol and lower. ZINC000103579839 demonstrated the lowest docking score with respect to VP40 (at −9 kcal/mol) among the TCM compounds, followed by ZINC000085531689 with a score of −8.9 kcal/mol. The compounds ZINC000014089759, ZINC000085545967, ZINC000085568633, ZINC000085593149, and ZINC000085991498 all had a docking score of −8.8 kcal/mol.

A total of 2738 approved drugs were successfully screened against the VP40 protein, of which 30 compounds had docking scores of −8 kcal/mol and lower. Doramectin had the lowest docking score of −9.1 kcal/mol, followed by ledipasvir with a docking score of −9 kcal/mol (Table 1). Avermectin B1 (abamectin) and elbasvir both had a docking score of −8.7, while venetoclax (ABT-199 or GDC-0199) and revefenacin both had a docking score of −8.5 kcal/mol (Table 1). Glecaprevir also had a docking score of −8.3 kcal/mol (Table 1). Doramectin and abamectin are avermectins, a class of macrocyclic lactone compounds that are widely used in the veterinary field for the treatment of parasites [60,61]. Furthermore, the antiviral activity of avermectins such as ivermectin and abamectin have been recorded in literature [62–67]. Abamectin and ivermectin were reported to inhibit Chikungunya virus (CHIKV) with EC$_{50}$ values of 1.5 and 0.6 µM, respectively [62]. They were also reported to have antiviral effects on alphaviruses (Semliki Forest and Sindbis virus) and yellow fever virus [62]. Yellow fever virus is a flavivirus, a small enveloped RNA virus, and Ebola is also an RNA virus [68,69]. Although flaviviruses and filoviruses have

different modes of transmission and symptoms, they may both be characterized by viral hemorrhagic fevers (VHFs) [68–70]. Ledipasvir and elbasvir are hepatitis C virus (HCV) NS5A inhibitors that help prevent viral RNA replication, assembly, and the viral release of HCV infection [71,72]. Glecaprevir is also an HCV NS3/4A protease inhibitor [73–75], making it an interesting candidate to test and repurpose for Ebola treatment. Venetoclax, a B-cell lymphoma 2 inhibitor [76,77] used in chronic lymphocytic leukemia and small lymphocytic lymphoma treatments [78,79], was shown to reduce latent virus in a T cell model when used in combination with ixazomib [80]. There have been cases where Ebola still persists in immune-privileged regions (including the eyes and testes) in survivors [81]. Experimental testing is required to determine if venetoclax could help reduce the viral load in immune-privileged sites after EVD treatment regimens are completed.

For the curated inhibitors, the docking scores ranged from −4.4 to −7.9 kcal/mol for the 43 successfully docked compounds. Nilotinib demonstrated the lowest docking score of −7.9 kcal/mol, followed by imatinib, cepharanthine, and daunomycin with docking scores of −7.6, −7.3, and −6.9 kcal/mol, respectively. Azarclorzine and mefloquine both had a docking score of −6.6 kcal/mol, while bosutinib, mebendazole, raloxifene, sangivamycin, sunitinib, and topotecan all had a docking score of −6.3 kcal/mol. Nilotinib and imatinib, which were used as standards in this study, have previously been shown to reduce VP40 in VLPs at the concentrations tested (10 and 20 μM) with insignificant toxicities [82].

An in silico study used AutoDock 4.2 to virtually screen five compounds (vindesine, BIX-01294, NVP-ADW742, ZINC91973695, and ZINC67869167) against VP40 [39]. These five compounds were experimentally shown to inhibit EBOV [39]. The docking scores of the five compounds ranged from −4 to −5 kcal/mol [39]. The docking score rankings of the five compounds from AutoDock 4.2 were consistent with their experimental half maximal inhibitory concentration (IC_{50}) rankings [39,83]. Another study also screened compounds in the MCULE database against VP40 using AutoDock Vina and the docking scores of the top compounds ranged from −5.9 to −7 kcal/mol [47]. Herein, the shortlisted compounds demonstrated better docking scores than those of previous studies [39,47]. The relatively better docking scores of the compounds reported herein make them interesting candidates for further investigation into their potential EBOV-VP40-binding and inhibition properties.

2.5. Absorption, Distribution, Metabolism, Excretion, and Toxicity (ADMET) Profiles of the Shortlisted Compounds

ADMET prediction was further performed on shortlisted compounds from the AfroDb, NANPDB, and TCM libraries to analyze their pharmacological profiles. It is essential for a parent compound to have an impressive ADMET profile. Lipinski's rule of five and Veber's rule were applied in the prediction of drug-like and physiochemical properties of the shortlisted compounds. These rules are a set of property values that were derived from the classification of the key physicochemical properties of drug-like compounds [84]. According to Lipinski's rule, a drug-like compound should have a molecular weight ≤500 Daltons; a logP value ≤5; a number of hydrogen bond donors ≤5; and a number of hydrogen bond acceptors ≤10 [85–87]. According to Lipinski, a compound is drug-like when it is within the acceptable range of the rule of five or when it violates only one of the rules. On the other hand, Veber's rule dictates that a good orally bioavailable drug should possesses 10 or fewer rotatable bonds and a topological polar surface area (TPSA) less than 140 Å^2 [88].

Based on Lipinski's rule, the compounds ZINC000095486217, ZINC000085594516, and ZINC000095486263 from the AfroDb library had two, two, and three violations, respectively, and were thus eliminated from further analyses. ZINC000028462577 was also predicted to violate Veber's rule, as it had a TPSA of 170.8 Å^2. Only three AfroDb compounds, namely, ZINC000034518176, ZINC000095485942, and ZINC000014825190, were in accordance with both Lipinski's and Veber's rules. For the NANPDB library, only NANPDB2933 was in accordance with both Lipinski's and Veber's rules (Table 2). NANPDB2933 has a molecular weight of 486.51 g/mol, a TPSA of 132.5 Å^2, and a consensus logP of 1.6 (Table 2). A total

of seven and ten compounds violated only Lipinski's and only Veber's rules, respectively, while seven violated both Lipinski's and Veber's rules. A total of 84 compounds out of the 163 TCM compounds with favorable docking scores complied with both Lipinski's and Veber's rules. The ADMET results of the shortlisted compounds are summarized in Tables 2 and S1.

Table 2. Physicochemical and biological properties of some of the shortlisted compounds predicted using SwissADME.

Compound	Docking Score (kcal/mol)	Molecular Weight (g/mol)	TPSA (Å²)	LogP	ESOL Solubility Class	GI Absorption	BBB Permeant	Pgp Substrate
			AfroDb					
ZINC000034518176	−8.1	426.72	20.23	7.03	Poorly soluble	Low	No	No
ZINC000095485942	−8.1	474.5	135.8	1.4	Soluble	High	No	Yes
			NANPDB					
NANPDB2933	−8.5	486.51	132.5	1.6	Soluble	High	No	Yes
			TCM					
ZINC000085531689	−8.9	568.66	105.86	2.57	Moderately soluble	High	No	Yes
ZINC000014089759	−8.8	470.68	74.6	5.36	Poorly soluble	High	No	Yes
ZINC000085545967	−8.8	580.79	118.22	4.14	Poorly soluble	High	No	Yes
ZINC000085568136	−8.7	598.66	100.74	4.98	Poorly soluble	High	No	Yes
ZINC000095912717	−8.7	544.59	134.66	1.59	Soluble	High	No	Yes
ZINC000014089743	−8.6	456.7	57.53	6.12	Poorly soluble	Low	No	No
ZINC000101564200	−8.6	478.49	115.06	4.69	Poorly soluble	Low	No	No
ZINC000085504890	−8.5	536.66	101.16	1.97	Moderately soluble	High	No	Yes
ZINC000095909661	−8.5	594.7	83.86	4.75	Poorly soluble	High	No	No
ZINC000070454124	−8.4	564.58	119.34	3.83	Moderately soluble	High	No	Yes
ZINC000085530485	−8.4	566.64	124.8	3.15	Moderately soluble	High	No	Yes
ZINC000095911418	−8.4	462.62	52.6	5.63	Moderately soluble	High	No	No

The compounds were further subjected to toxicity testing using OSIRIS DataWarrior 5.5.0 [89]. ZINC000014825190 (AfroDb) was predicted to have low tumorigenic and high reproductive effects and was thus eliminated. ZINC000034518176, ZINC000095485942, and NANPDB2933 were predicted to be non-tumorigenic, non-mutagenic, and non-irritants and had no reproductive effects. For the TCM library, a total of 41 out of the 84 top compounds were predicted to be less toxic, with no mutagenic, tumorigenic, irritancy-inducing, or reproductive effects. ZINC000085568633, with a docking score of −8.8 kcal/mol, was predicted to be highly tumorigenic, while ZINC000085991498 (which also had a docking score of −8.8 kcal/mol) was predicted to have low-level mutagenic effects. In all, 43 compounds from the 3 natural product libraries (1 NANPDB, 2 AfroDb, and 41 TCM compounds) were shortlisted as potentially safe binders of the VP40 NTD. The ADMET predictions indicate that the shortlisted compounds have desirable ADMET properties with insignificant toxicity.

2.6. Protein–Ligand Interactions of Lead Compounds

Visualizing the protein–ligand complexes of the top compounds in PyMOL showed that all the shortlisted ligands had docked deep into the active sites. Further analysis was carried out to identify the amino acid residues of the VP40 protein that interact with the ligands by using Ligplot+ to visualize the interactions (Figures 3 and S2a–j). ZINC000034518176 docked at the RNA binding site, interacted with Gly139 (with a bond length of 3.05 Å) via hydrogen bonds, and formed hydrophobic bonds with Phe36, Asn43, Pro47, Thr121, Phe125, Arg134, Asn136, Arg137, and Leu138 (Table 1 and Figure S2a). The other shortlisted compounds were observed to bind in the loop region. It was observed that ZINC000085568136, ZINC000070454124, ledipasvir, elbasvir, revefenacin, nilotinib, and imatinib docked in the same site on the loop region (Table 1). Nilotinib did not form any hydrogen bonds with VP40 (Table 1). However, nine hydrophobic interactions were

observed for the VP40–nilotinib complex, namely, with the Tyr18, Arg21, Pro39, Val42, Gly44, Gly126, Lys127, Ala128, and Thr129 residues (Figure 3a and Table 1).
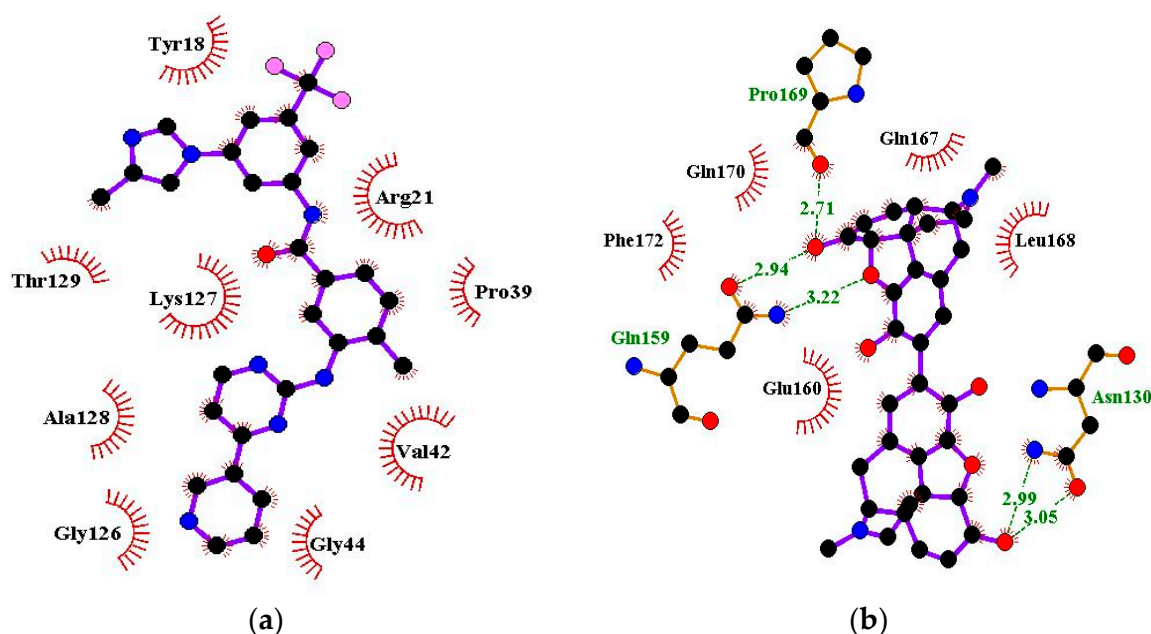
Figure 3. Protein–ligand interaction map of VP40 in complex with (**a**) nilotinib and (**b**) ZINC000085531689. The green, dotted lines indicate hydrogen bonds while the red arcs with spikes represent hydrophobic interactions.

Most of the top compounds were observed to dock in the loop region surrounded by the Lys127, Ala128, Thr129, Asn130, Pro131, Gln159, Glu160, Pro164, Pro165, Val166, Gln167, Leu168, Pro169, and Gln170 residues. ZINC000085531689, with a docking score of −8.9 kcal/mol, formed hydrogen bonds with Asn130 (2.99 and 3.05 Å), Gln159 (2.94 and 3.22 Å), and Pro169 (2.71 Å) and interacted with the Glu160, Gln167, Leu168, Gln170, and Phe172 residues via hydrophobic bonds (Table 1 and Figure 3b). According to the interaction maps, doramectin, which had the lowest docking score with respect to VP40 (−9.1 kcal/mol), also formed five hydrogen bonds with Glu12, Asn130, Gln159, Leu168, and Pro169 with bond lengths of 2.72, 3.14, 2.8, 3.33, and 3.06 Å, respectively (Table 1 and Figure S2h). Doramectin also interacted via hydrophobic bonding with Tyr13, Lys127, Ala128, Thr129, Pro131, Glu160, Phe161, Pro165, and Gln170 (Table 1 and Figure S2h). The overlapping L-budding domains consisting of residues 7PTAPPEY13 have been experimentally reported to interact with host cellular WW domain proteins including Nedd4, Tsg101, AIP1/Alix, and HECTD1 [49–51]. Interactions with these residues regulate the budding and egress of Ebola-virus-like particles (VLPs) from host cells [50,51].

The compounds ZINC000014089759 and ZINC000014089743 were also observed to bind in a different area on the loop region, forming hydrophobic interactions with Tyr13, Tyr18, Pro19, Asn23, and Leu127 (Table 1). ZINC000014089759 also formed hydrogen bonds with Arg21 (3.02, 3.03 Å), Pro39 (3.1 Å), and Lys127 (3.04 Å) (Figure S2d) while ZINC000014089743 interacted via hydrogen bonds with Arg21 (2.96 Å), Ser24 (2.97 Å), and Pro39 (3.09 Å). In the loop region, Lys127 was observed to be involved in the VP40–ligand interaction.

A recent in silico study reported that the topmost compound interacted with the following residues: Thr123, His124, Phe125, Gly126, Lys127, Arg134, and Tyr171 [47]. In another study, vindesine was predicted to form hydrogen bonds with Gln35, Gln38, and Lys127 [39]. BIX-01294 was also shown to interact with Gln33 and Ile34, while NVP-ADW742 interacted with Lys127 via a hydrogen bond. Lys127 was suggested to play a critical role in ligand binding [39].

2.7. Prediction of Biological Activities of Lead Compounds

Even though molecular docking studies can provide valuable insights into the poses and interactions between molecules and their targets, without experimental validation, it is difficult to determine the true accuracy of the predictions. In the midst of this lacuna, this study employed additional computational approaches to mitigate the potential errors in the molecular docking process. In this study, the biological activity of the shortlisted compounds was predicted using a Bayesian algorithm [90–93]. The anti-EBOV inhibition efficiencies of the compounds were also predicted using RF and SVM models [94]. Structural similarity searches of the shortlisted compounds were also performed to identify compounds with known antiviral or anti-EBOV related activity. Structural features are often critical determinants of biological activity, and, in many cases, compounds with structural features similar to known active compounds can exhibit similar biological activity [95,96].

2.7.1. PASS Predictions

The biological activity spectrum (BAS) of a compound is a characteristic that reflects the compound's various pharmacological effects and its physiological and biochemical mechanisms of action [90]. A BAS also accounts for specific toxicities such as mutagenicity, carcinogenicity, teratogenicity, and embryo toxicity [90]. This prediction operates on the principle that the biological activity of a compound equates to its structure; therefore, this activity is largely dependent on the structural nature of a compound. The majority of biologically active compounds have both pharmacotherapeutic and side-effect-inducing/toxic actions. The biological activity of a compound gives insight into its mechanism of action against a therapeutic target.

In this study, PASS was employed to predict the biological activities of the analyzed potential lead compounds [90–93]. The compounds ZINC000034518176, ZINC000085531689, ZINC000014089759, ZINC000085545967, ZINC000014089743, and ZINC000101564200 were predicted to be antivirals with anti-influenza activity, exhibiting Pa values of 0.793, 0.214, 0.739, 0.243, 0.241, and 0.356 and Pi values of 0.003, 0.176, 0.004, 0.140, 0.115, and 0.062, respectively. The compounds were also predicted to possess other antiviral activities, including against rhinovirus, herpes, HIV, and hepatitis B, with their Pa values greater than their Pi values. ZINC000101564200 and ZINC000014089743 were also predicted to be human coronavirus 3C-like protease inhibitors with Pa values of 0.270 and 0.249 and Pi values of 0.050 and 0.078, respectively. ZINC000101564200 was further predicted to be an inhibitor of simian immunodeficiency virus proteinase (Pa: 0.318 and Pi: 0.105) and HIV-1 integrase and possesses antiviral properties against adenoviruses (Pa: 0.391; Pi: 0.033), picornaviruses (Pa: 0.353; Pi: 0.155), cytomegalovirus (CMV) (Pa: 0.243; Pi: 0.087), and poxviruses (Pa: 0.216; Pi: 0.135).

Furthermore, NANPDB2933, ZINC000085531689, ZINC000014089759, ZINC000085545967, ZINC000014089743, and ZINC000101564200 were predicted to be RNA synthesis inhibitors. Favipiravir, a selective RdRp (RNA polymerase) inhibitor, exhibits activity against single-stranded RNA viruses (including EBOV) by inhibiting viral replication [2,97–99]. ZINC000034518176 and ZINC000101564200 were also predicted to be viral entry inhibitors. Enfuvirtide, a peptide used for HIV treatment, is a viral entry inhibitor [100,101]. LJ001 is a viral entry small molecule inhibitor that has been shown to be effective against a wide range of enveloped viruses [102]. Enveloped viruses such as EBOV, HIV, and coronaviruses have been reported to have similar cell fusion mechanisms [100]. These predictions provide evidence for the antiviral properties of the shortlisted compounds, rendering them interesting candidates for further in vitro probing.

NANPDB2933, ZINC000085531689, ZINC000014089759, and ZINC000085545967 were predicted to be antihemorrhagic. Antihemorrhagic agents may help reduce the risk of bleeding and improve survival rates in patients with severe Ebola infection. ZINC000034518176, ZINC000095485942, NANPDB2933, ZINC000014089759, ZINC000085545967, ZINC000014089743, and ZINC000101564200 were also predicted to be hepatoprotectants with Pa values of 0.926, 0.377, 0.282, 0.929, 0.429, 0.932, and 0.317 and Pi values of 0.002,

0.036, 0.066, 0.002, 0.027, 0.002, and 0.054, respectively. Liver damage is one of the hallmarks of EVD infection [103–105]. These compounds may be beneficial with respect to managing liver failure and may support the liver during recovery from EVD.

2.7.2. Structural Similarity Search

A structural similarity search of the potential lead compounds via DrugBank [106,107] revealed that ZINC000034518176 is structurally similar to ginsenosides and beta-sitosterol with scores of 0.705 and 0.785, respectively. Ginsenosides, the main active ingredients in ginseng, are widely known for their antiviral properties [108–112]. β-sitosterol (50 mg/kg), the main component of *Pinellia ternata* (Thunb.) Breit., was reported to inhibit ~95.79% of white spot syndrome virus (WSSV) in crayfish [113]. In addition, the stem bark, root, and leaf extracts of *Erythrostemon yucatanensis* (Greenm.) Gagnon and GP Lewis were reported to have anti-influenza-virus activity [114]. Analysis of spectroscopy data revealed that a combination of three phytosterols, namely, β-sitosterol, stigmasterol, and campesterol, in the stem bark active fraction was responsible for attenuating hemagglutinin binding and affected viral particle infectivity (IC$_{50}$ of 3.125 μg/mL) [114].

ZINC000034518176, ZINC000014089759 (11-keto boswellic acid), and ZINC000014089743 are also structurally similar to ursolic acid, presenting similarity scores of 0.736, 0.761, and 0.882, respectively. Ursolic acid has been shown to possess broad spectrum antiviral activity [115,116]. Ursolic acid (10 μM) was reported to inhibit rotavirus replication with no cytotoxicity in MA104 cells [117]. Ursolic acid, an extract of the Chinese herb *Fructus Ligustri Lucidi*, was reported to inhibit HCV (JFH1) at an IC$_{50}$ of 10.6 μg/mL [118].

ZINC000014089743 was predicted to be structurally similar to madecassic acid (0.863), asiatic acid (0.863), enoxolone (0.807), and betulinic acid (0.701). Madecassic acid and asiatic acid (up to 10 μM) showed moderate and weak inhibitory activities, respectively, against HIV-1 viral protein R [119]. Enoxolone (glycyrrhetinic acid (GA)) is a hepatoprotective agent that inhibited the activation of hepatic inflammation in a hepatitis-virus-infected mouse [120]. Four derivatives of GA were shown to inhibit hepatitis B DNA replication with IC$_{50}$ values less than 10 μM while GA had an IC$_{50}$ of 39.28 μM [121]. GA's anti-SARS-CoV-2 [122,123], anti-influenza [124], and anti-Epstein–Barr virus [125] activities have been reported previously. Betulinic acid has been reported to possess antiviral properties. It was reported to inhibit dengue virus 2 (DENV2) in Huh7, HepG2, HEK293T, BHK-21, and Vero cells with IC$_{50}$ values of 0.9463, 0.8038, 0.9463, 0.7697, and 3.224 μM, respectively [126]. Betulinic acid (IC$_{50}$ < 2 μM) also inhibited three other serotypes of DENV: DENV1, DENV3, and DENV4 [126]. The inhibition of ZIKV (in JEG-3 cells) and CHIKV (in SJCRH30 cells) with IC$_{50}$ values of 2.45 and 0.6853 μM, respectively, was also reported [126]. The anti-influenza [127], anti-SARS-CoV-2 [128], anti-hepatitis [129,130] anti-HIV [131,132], and anti-herpetic [133] activities of betulinic acid have also been highlighted in the literature.

ZINC000101564200 is structurally similar to anthralin (0.754) and emodin (0.711). Anthralin suppresses influenza A virus (IAV) proliferation [134] and has been shown to be an HIV-latency-reversing agent [135]. Therefore, ZINC000101564200 may be useful for EBOV latency reversal to completely eradicate EBOV from patients' bodies. Emodin has been reported to have virucidal effects on Zika virus (ZIKV) in which it provokes a reduction in viral load of 83.3% at 40 μM [136]. Emodin also possesses anti-IAV [137–139], anti-CMV [140], and anti-HBV [141] properties. The results from our structural similarity search corroborate the likelihood of the shortlisted compounds being potential antivirals.

2.7.3. Anti-Ebola Activity Prediction

The anti-EBOV inhibition efficiencies of the shortlisted compounds were predicted via RF and SVM models using Anti-Ebola [94]. Anti-Ebola is a regression-based prediction algorithm that predicts the potential EBOV-inhibitory activity of a query compound using quantitative structure–activity relationship (QSAR) analysis [94]. These models were previously validated using compounds that have been experimentally shown to possess anti-EBOV activity [94]. The model predicted that indinavir (0.03 μM), maraviroc

(0.30 µM), abacavir (1.27 µM), tilorone (1.95 µM), pyronaridine (0.5 µM), and quinacrine (2 nM) were anti-EBOV compounds [94], and these results are consistent with experimental findings [142,143].

In this study, the compounds ZINC000034518176 and ZINC000095485942 from the AfroDb library were predicted by the RF model of Anti-Ebola [94] to have IC_{50} values of 3.86 and 2.93 µM, respectively, while the SVM model predicted IC_{50} values of 3.14 and 20.15 µM, respectively (Table S2). Both models predicted that NANPDB2933 had an IC_{50} of 2 µM (Table S2). The compounds whose inhibition efficacy could not be predicted were automatically eliminated. Anti-Ebola was not able to predict the inhibitory efficiency of ZINC000085504890 and ZINC000070451048 from the TCM library. In addition, the Ebola inhibition efficiencies of venetoclax, hederacoside C, pibrentasvir, and efonidipine (approved drugs library) could not be predicted. However, revefenacin, BMS-927711 (BHV-3000), and irinotecan (CPT-11) were predicted to show no anti-Ebola activity [IC_{50} of 1×10^6 µM (1×10^3 mM or 1 M)] by both the RF and SVM models and were thus removed from the shortlisted compounds (Table S2). Irinotecan, a DNA topoisomerase I inhibitor, was previously reported to have no antiviral effect on pseudorabies virus (PRV) infection [144], thereby lending support to the prediction that these compounds likely do not have any anti-Ebola properties.

Sennoside A was recently shown to inhibit Zika virus protease with IC_{50} and Ki values of 0.66 and 0.19 µM, respectively [145]. Sennoside A and B also inhibited HIV-1 ribonuclease H and reverse-transcriptase-associated DNA polymerase activities with IC_{50} values in the 2–5 µM range [146]. In this study, sennoside A and B, which are both anthraquinone glycosides [147], were predicted to be potential anti-EBOV compounds with IC_{50} values below the micromolar range (Table S2). Similarly, ledipasvir, avermectin B1, nafarelin acetate, danoprevir (ITMN-191), eltrombopag, lanatoside C, glycyrrhizin (glycyrrhizic acid), and daclatasvir digydrochloride were also predicted to possess anti-EBOV properties in very low micromolar ranges (Table S2). The broad spectrum antiviral activity of lanatoside C has been reported [148]. Lantoside C was identified as being able to effectively inhibit all four serotypes of dengue (with an IC_{50} of 0.19 µM in HuH-7 cells), Kunjin, Chikungunya, and Sindbis and the human enterovirus 71 viruses [148]. Like ledipasvir, danoprevir is a known directly acting antiviral used in the treatment of chronic HCV infection [149–151]. Eltrombopag is known to increase platelet counts in HCV-associated thrombocytopenia [152,153] and can be beneficial in the management of bleeding in cases of Ebola, a viral hemorrhagic fever. Some EVD patients have been reported to experience thrombocytopenia [154,155]. Glycyrrhizin's wide range of antiviral properties has been documented in literature [156–160]. These predictions and the antiviral-related properties of these compounds make them interesting candidates for experimentally probing to determine their anti-EBOV activity and selectivity.

2.8. Molecular Dynamics Simulations of Some Selected Compounds

MD simulations are used not only to explore the conformational aspects of biological systems but also to obtain a significant scope with which to analyze protein–ligand interactions. A 100 ns MD simulation was performed to investigate the dynamic behavior of the lead complexes. The simulation was conducted for the unbound protein (VP40), nilotinib, and seven potential lead compounds complexed with VP40.

2.8.1. Root-Mean-Squared Deviation (RMSD)

To explore the intricate interactions between VP40 and the analyzed ligands and investigate the stability of the lead complexes, the RMSD was analyzed for the 100 ns MD simulation. The VP40–ZINC000034518176 complex demonstrated the greatest stability among all the systems, presenting an average RMSD of 0.33 ± 0.039 nm. The unbound VP40 protein had an average RMSD of 0.37 ± 0.048 nm. VP40 in complex with nilotinib, ZINC000085568136, ZINC000085531689, ZINC000095912717, and ZINC000014089759 presented average RMSD values of 0.404 ± 0.051, 0.45 ± 0.077, 0.39 ± 0.057, 0.37 ± 0.045,

and 0.37 ± 0.046 nm, respectively. All the systems were observed to reach equilibrium around 25–35 ns (Figure 4). The VP40–ZINC000085568136 complex demonstrated the highest RMSD, which reached 0.5 nm around 40 ns and was maintained until the end of the 100 ns simulation period (Figure 4). Similar RMSD values (~0.45 to 0.48 nm) were reported previously for the top two compounds (emodin-8-beta-D-glucoside and tonkinochromane G) identified via virtual screening and MD simulations of VP40 [9]. The relatively higher RMSD values obtained for VP40 are not surprising, as loop regions or proteins with more loops tend to have higher RMSD values than alpha helices and beta sheets [161].
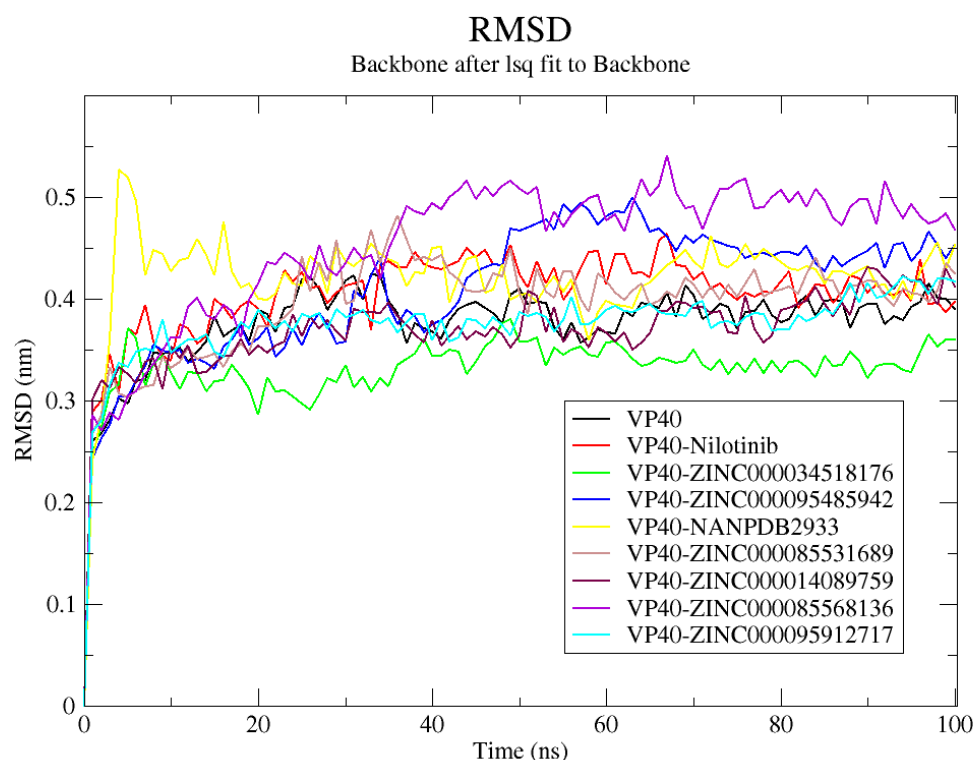
Figure 4. RMSD plot of the EBOV VP40 and VP40–ligand complexes after 100 ns MD simulations. The unbound VP40 protein, VP40–nilotinib, VP40–ZINC000034518176, VP40–ZINC000095485942, VP40–NANPDB2933, VP40–ZINC000085531689, VP40–ZINC000014089759, VP40–ZINC000085568136, and VP40–ZINC000095912717 complexes are colored black, red, green, blue, yellow, brown, maroon, violet, and cyan, respectively.

2.8.2. Root Mean Square Fluctuations (RMSF)

The RMSF of each complex was analyzed to investigate each residue's average fluctuation throughout the 100 ns simulation (Figure S3). The RMSF provides information on residues that are involved in ligand binding, as these residues tend to have lower fluctuations due to their interactions with the ligand that stabilizes the complex. In many cases, binding interactions can stabilize the region and reduce the flexibility of residues involved in binding. For all the VP40–ligand complexes, fluctuations were observed at similar regions of VP40 (Figure S3). Major fluctuations were observed at 1–50, 60–72, and 125–131, while minor fluctuations were observed at residue indexes of 80–94, 101–110, and 140–145 (Figure S3). The highest RMSF was observed for the VP40–NANPDB2933 complex at residue index 29–36 with values ranging from 0.5826 nm (Gly35) to 0.9188 nm (Asn31). The Gly29, Gly30, Ser32, Asn33, Thr34, and Phe36 residues had RMSF values of 0.8307, 0.8799, 0.804, 0.7405, 0.6474, and 0.7089 nm, respectively, for the VP40–NANPDB2933 complex (Figure S3). Positions 72–80, 95–100, 119–122, and 172–183 demonstrated the lowest fluctuations (Figure S3). These residue indexes could be involved in ligand binding and warrant further investigation.

2.8.3. Radius of Gyration (Rg)

The compactness of the complexes was assessed by analyzing the radius of gyration (Figure 5). A steady radius of gyration throughout a simulation period indicates a stably folded protein [162]. The Rg for the unbound protein was relatively steady over the simulation period, corresponding to an average of 1.67 ± 0.01 nm (Figure 5). All the VP40–ligand complexes had Rg values comparable to that of the unbound protein. The VP40–nilotinib, VP40–ZINC000014089759, VP40–ZINC000034518176, and VP40–ZINC000095485942 complexes had average Rg values lower than that of the unbound VP40, presenting values of 1.668 ± 0.025, 1.653 ± 0.01, 1.638 ± 0.018, and 1.635 ± 0.012 nm, respectively (Figure 5). The VP40–ZINC000085568136, VP40–ZINC000085531689, VP40–ZINC000095912717, and VP40–NANPDB2933 complexes exhibited comparable Rg scores, presenting average values of 1.683 ± 0.015, 1.685 ± 0.016, 1.685 ± 0.01, and 1.681 ± 0.023 nm, respectively (Figure 5).
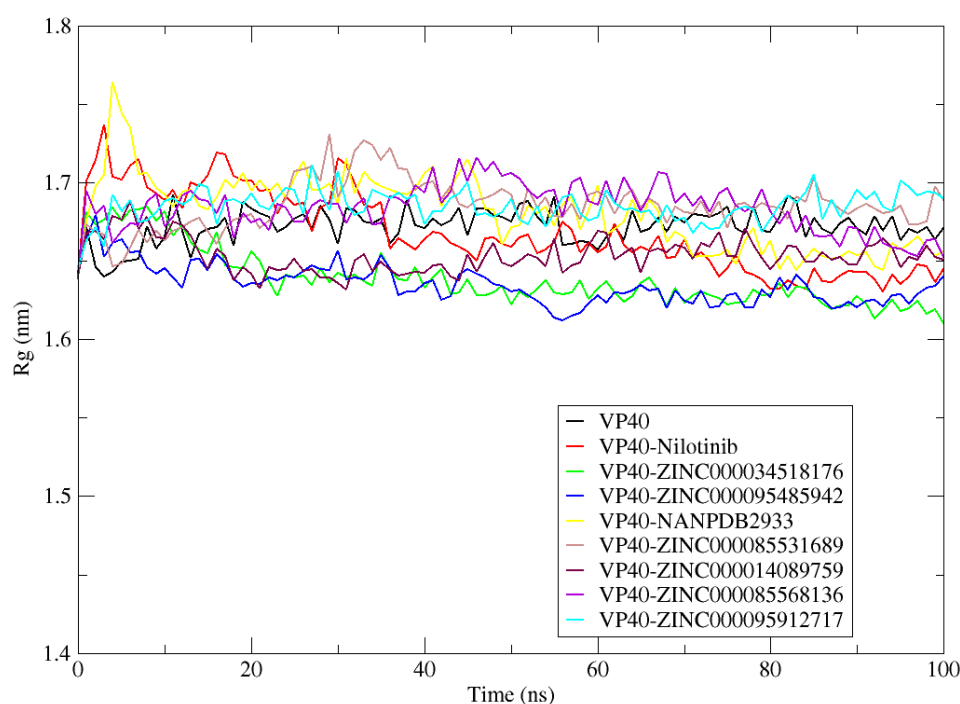
Figure 5. Rg plot of the EBOV VP40 and VP40–ligand complexes after 100 ns MD simulations. The unbound VP40 protein, VP40–nilotinib, VP40–ZINC000034518176, VP40–ZINC000095485942, VP40–NANPDB2933, VP40–ZINC000085531689, VP40–ZINC000014089759, VP40–ZINC000085568136, and VP40–ZINC000095912717 complexes are colored black, red, green, blue, yellow, brown, maroon, violet, and cyan, respectively.

2.8.4. Hydrogen Bond Analysis

The hydrogen bonds formed between VP40 and the studied ligands were analyzed using "gmx hbond". The number of hydrogen bonds formed at every nanosecond was determined. Snapshots taken at 25 ns intervals (0, 25, 50, 75, and 100 ns) for each system during the 100 ns MD simulations were also generated, and the interaction profiles were determined using LigPlot+ (v1.4.5) (Table S3). On average, the VP40–nilotinib, VP40–ZINC000095485942, VP40–NANPDB2933, VP40–ZINC000085531689, VP40–ZINC000014089759, VP40–ZINC000085568136, and VP40–ZINC000095912717 complexes had 0.634 ± 0.784, 0.257 ± 0.56, 2.693 ± 1.046, 1.446 ± 1.22, 0.139 ± 0.347, 0.782 ± 0.701, and 1.337 ± 0.886 hydrogen bonds, respectively, throughout the simulation period. ZINC000034518176, on the other hand, was observed to form no hydrogen bonds with VP40 throughout the 100 ns period. However, the interaction maps showed that ZINC000034518176 formed only one

hydrogen bond with Gly139 (bond length of 3.02 Å) at the 0 ns timeframe but could not maintain this interaction throughout the simulation period (Table S3).

According to "gmx hbond", the highest number of hydrogen bonds (five H bonds) formed were observed for VP40–ZINC000085531689 (at time = 0 ns) and NANPDB2933 (at 23 ns and 66 ns). However, the interaction maps revealed that ZINC000085531689 formed six hydrogen bonds with Asn130 (2.79, 3.16, and 3.24 Å), Gln159 (3.02 Å), Glu160 (2.53 Å), and Pro169 (2.63 Å) and interacted via hydrophobic interactions with Gln167, Leu168, Gln170, and Phe172 at 0 ns (Table S3). NANPDB2933 interacted with His124 (2.91 Å), Val166 (3.03 and 3.28 Å), and Leu168 (3.25 Å) via hydrogen bonds and formed hydrophobic bonds with Met89, Ala128, Thr129, Asn130, Pro131, Glu160, Pro164, Pro165, Gln167, and Phe172 at 25 ns. At 50 ns, hydrogen bond interactions with Val166 (2.88 and 3.25), Leu168 (3.2 and 3.34 Å), and Gln170 (2.85 Å) were observed (Table S3).

At the end of the simulation, "gmx hbond" showed that NANPDB2933, ZINC000095485942, and ZINC000085531689 formed three, one, and one hydrogen bonds with VP40, respectively, while the other ligands lost their hydrogen bonds with VP40 (Figure S4). According to the interaction profile, at the end of the simulation (100 ns), NANPDB2933 formed four hydrogen bond interactions with Asn130 (3.05 Å), Val166 (2.79 and 3.31 Å), and Gln170 (2.73 Å) and formed hydrophobic interactions with His124, Ala128, Thr129, Pro131, Val133, Glu160, Leu163, Leu168, and Phe172 (Table S3). The hydrogen bonds formed between NANPDB2933 and VP40 could influence the complex's binding properties and stability and the potential activity of NANPDB2933 since multiple hydrogen bonds have been reported to contribute to ligand activity [163]. In addition, ZINC000095485942 formed two hydrogen bonds with Met1 (2.52 and 2.78 Å), while ZINC000085531689 also formed two hydrogen bonds with Glu160 (2.95 Å) and Gln167 (3.32 Å) at 100 ns (Table S3).

2.9. Evaluation of Lead Compounds Using MM/PBSA Computations

2.9.1. Contributing Energy Terms

MM/PBSA calculations were performed to evaluate the binding free energies of the VP40–ligand complexes after the MD simulation [164,165]. The strength of the interaction between a protein and a ligand is quantified by its binding free energy. The known inhibitor, nilotinib, had a binding free energy of −11.21 kJ/mol according to the MM/PBSA calculations (Table 3). All the potential lead compounds demonstrated lower binding free energies than nilotinib, implying that they may have higher binding affinity for VP40 than nilotinib (Table 3). The binding free energy values of the VP40–potential lead complexes ranged from −46.97 kJ/mol to −118.9 kJ/mol, with NANPDB2933 showing the highest affinity to VP40 (Table 3). The very high binding affinity demonstrated by NANPDB2933 is not surprising, as it demonstrated the most developed hydrogen bond network with VP40 (Figure S4). The VP40–ZINC000034518176, VP40–ZINC000095485942, VP40–ZINC000085568136, VP40–ZINC000014089759, VP40–ZINC000095912717, and VP40–ZINC000085531689 complexes had binding free energies of −105, −103.3, −92.71, −70.52, −66.99, and −46.97 kJ/mol, respectively (Table 3). The relatively low standard deviation values of the binding free energies (<4 kJ/mol) signify the reliability of the simulations (Table 3).

Table 3. Contributing energies of the VP40–ligand complexes estimated from MM/PBSA computation. Values are presented as average energy value ± standard deviation in kJ/mol.

Compound	vdW	Electrostatic	Polar Solvation	SASA	Binding
ZINC000034518176	−117 ± 1.444	−33.3 ± 2.86	60.3 ± 2.132	−15.15 ± 0.164	−105 ± 1.815
ZINC000095485942	−93.49 ± 2.464	−80.21 ± 5.726	82.09 ± 6.387	−11.64 ± 0.257	−103.3 ± 2.217
NANPDB2933	−166.5 ± 1.572	−50.07 ± 1.021	114.5 ± 1.085	−16.84 ± 0.098	−118.9 ± 1.838
ZINC000085531689	−108.9 ± 2.797	−47.25 ± 4.294	123.2 ± 5.171	−14.06 ± 0.333	−46.97 ± 3.062
ZINC000014089759	−97.39 ± 3.274	15.76 ± 2.801	23.02 ± 1.793	−12.08 ± 0.395	−70.52 ± 2.343
ZINC000085568136	−156.5 ± 2.969	−28.37 ± 1.995	110.9 ± 2.643	−18.6 ± 0.306	−92.71 ± 2.553
ZINC000095912717	−131.9 ± 1.218	−21.38 ± 1.359	101.9 ± 1.817	−15.76 ± 0.147	−66.99 ± 1.73
Nilotinib	−108.5 ± 3.918	41.83 ± 5.391	71.17 ± 4.661	−15.75 ± 0.56	−11.21 ± 3.55

2.9.2. Energy Decomposition per Residue

The energies contributed by each residue were computed using MM/PBSA calculations to show the key residues that are involved in VP40–ligand binding (Figures 6 and S5) [164,166]. Residues with energy contribution values <−5.0 or >5.0 kJ/mol are critical in the binding of a ligand to a protein [167]. Residues contributing <−5.0 kJ/mol improve ligand binding while those with energy levels >5.0 kJ/mol impair binding potency. For the VP40–nilotinib complex, Met1 (20.53 kJ/mol), Arg2 (22.31 kJ/mol), Arg3 (18.97 kJ/mol), Arg21 (43.2 kJ/mol), Arg28 (26.68 kJ/mol), Arg52 (21.38 kJ/mol), His64 (16.91 kJ/mol), Lys86 (20.28 kJ/mol), Lys90 (18.33 kJ/mol), Lys104 (15.86 kJ/mol), Lys127 (42.41 kJ/mol), Arg134 (41.27 kJ/mol), Arg137 (24.97 kJ/mol), Arg148 (25.69 kJ/mol), Arg151 (28.08 kJ/mol), and Lys180 (18.36 kJ/mol) were observed to contribute unfavorably to ligand binding (Figure S5a). On the other hand, Glu12 (−27.69 kJ/mol), Glu15 (−29.69 kJ/mol), Glu40 (−43.26 kJ/mol), Val42 (−9.368 kJ/mol), Asp45 (−37.24 kJ/mol), Asp56 (−17.77 kJ/mol), Asp57 (−15.92 kJ/mol), Asp60 (−15.25 kJ/mol), Glu76 (−19.97 kJ/mol), Asp102 (−17.88 kJ/mol), Asp109 (−17.05 kJ/mol), Asp144 (−22.43 kJ/mol), Glu160 (−24.67 kJ/mol), Asp175 (−23.27 kJ/mol), Asp193 (−15.84 kJ/mol), and Asp194 (−32.22 kJ/mol) contributed favorably to nilotinib's binding (Figure S5a). Apart from Met1, all the residues that contributed positive energies were amino acids with positively charged side chains (Arg, His, and Lys), while those that contributed favorable (negative) energies had negatively charged side chains (Glu and Asp). Similar patterns were observed for ZINC000085531689 (Figure S5d) and ZINC000014089759 (Figure S5e). However, for ZINC000034518176 (Figure S5b) and ZINC000095485942 (Figure S5c), which were both obtained from the AfroDb library, the opposite pattern was observed. For ZINC000034518176 and ZINC000095485942, amino acid acids with positively charged side chains (except Met and Pro) contributed favorably to ligand binding, while those with negatively charged side chains contributed positive energy values. These residues may be considered key residues and may play major roles in ligand binding.
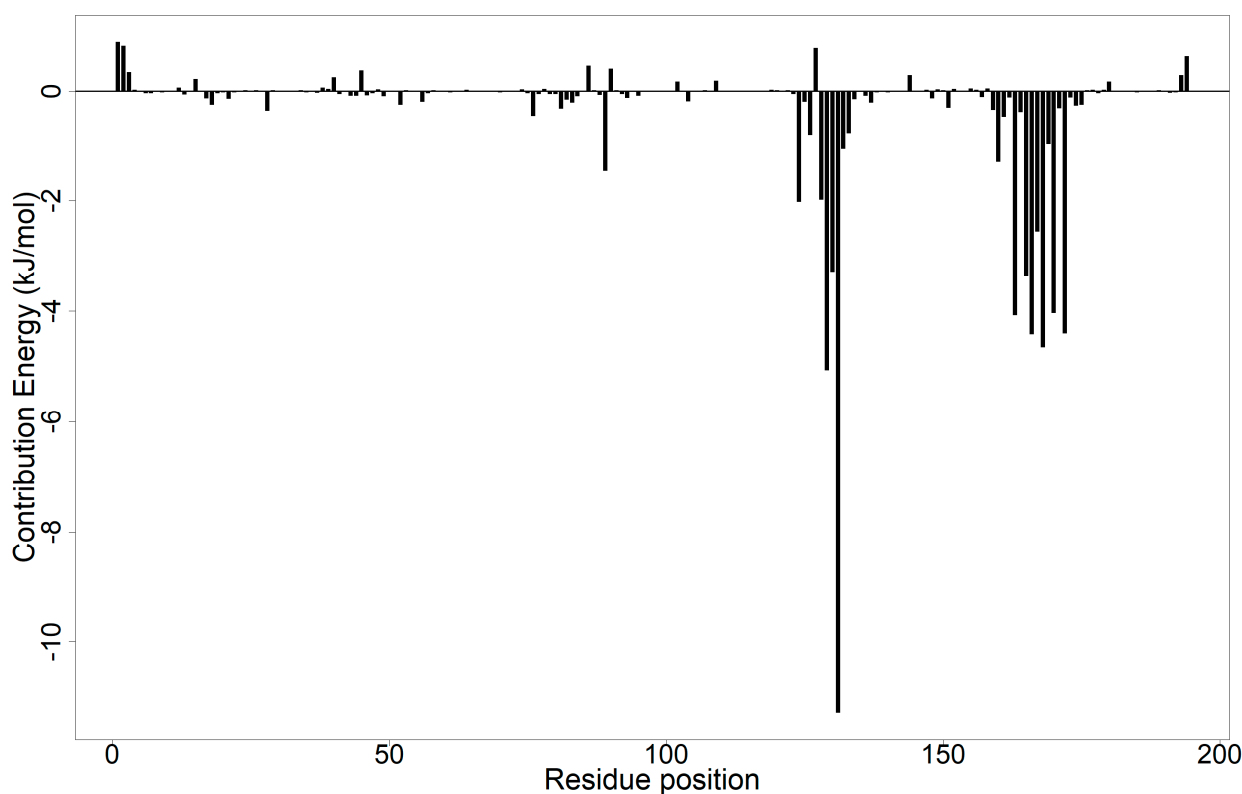
Figure 6. Per-residue energy decomposition plot of the VP40–NANPDB2933 complex showing the energy contributions of each amino acid residue.
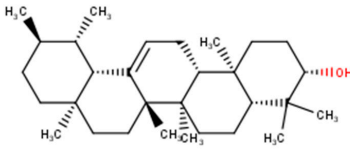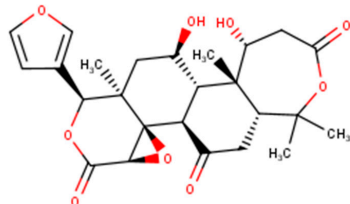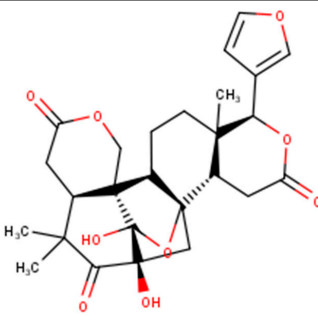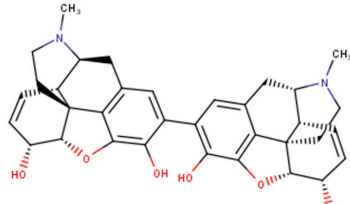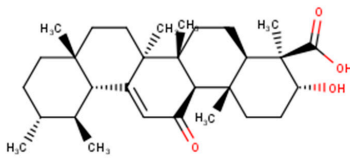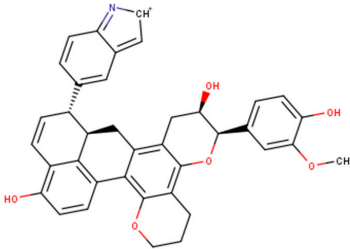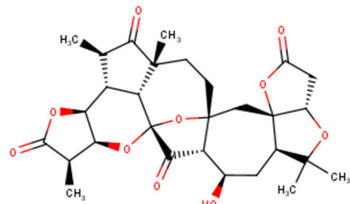
Regarding ZINC000085568136, only Gln170 and Tyr171 were observed to contribute significantly, presenting energy values of -8.598 and -11.8 kJ/mol, respectively (Figure S5f). Pro131 (-5.281 kJ/mol) and Glu160 (7.041 kJ/mol) were observed for ZINC000095912717 (Figure S5g), while Thr129 (-5.07 kJ/mol) and Pro131 (-11.29 kJ/mol) contributed significantly toward NANPDB2933 binding (Figure 6). The residues at positions 129–131 and 163–172 contributed favorably to NANPDB2933 binding (Figure 6). Future VP40 drug discovery studies can design compounds with stronger affinity to VP40 by taking these residues into consideration during lead optimization. The chemical mutation of the ligands [168] and the optimization of the partial charges [169,170] of the shortlisted molecules are strategies that can be exploited to improve the binding potency of the compounds in the binding site. Chemical mutation involves the modification of a compound's chemical structure through the introduction of new functional groups, the substitution of existing ones, or the modification of the compound's chemical scaffold. Pyridinations, fluorinations, and oxygen-to-sulfur mutations are some common chemical mutations that can be applied to ligands [168] to improve their affinity for specific amino acid residues.

2.10. Origin and Sources of the Potential Lead Compounds

Several compound databases, including Zinc15 [171], PubChem [172,173], ChEMBL [174–176], LOTUS [177], Indian Medicinal Plants, and Phytochemistry and Therapeutics (IMPPAT) [178], were searched for information on the seven shortlisted potential lead compounds (Table 4). The existing literature on the biological activity of the sources of the compounds was also investigated. NANPDB2933 (2-hydroxyseneganolide), which offers strong antifeedant activity (200 µg/mL and above) [179,180], has been extracted from the fruit [181] and stem bark [179,180] of *Khaya senegalensis*. *K. senegalensis* extracts possess antimicrobial, anti-cancer, and anti-inflammatory activity [182,183]. ZINC000095912717 (lancifodilactone C) is also available in *Schisandra chinensis* (Turcz.) Baill [184] and *Schisandra lancifolia* [185]. Lancifodilactone I to N, isolated from *S. lancifolia*, have previously been shown to possess anti-HIV-1 activity with an EC$_{50}$ ranging from 76.6 to 100.0 µg/mL [186]. Lancifodilactone I and C are structurally similar [186], thus rendering lancifodilactone C an interesting candidate to test experimentally to ascertain its anti-EBOV and antiviral properties.

ZINC000034518176, similar to α-amyrin, is a chemical constituent of *Vernonanthura chamaedrys* [187,188], *Mangifera indica* [189], *Cadia purpurea* [190], *Calendula officinalis* [191], *Pinalia leucantha* [192], *Ilex aquifolium* [193], *I. goshiensis* [194], and *Rhodomyrtus tomentosa* [195] according to Wikidata (https://www.wikidata.org/wiki/Q105000762 (accessed on 15 March 2023)) [196,197]. The organic extract of dried flowers from *Calendula officinalis* exhibits anti-HIV-1 replication properties and is non-toxic to human lymphocytic Molt-4 cells [198]. At 500 µg/mL, this organic extract protected uninfected Molt-4 cells for up to 24 h from infected U-937/HIV-1 cells [198]. ZINC000014089759 (11-keto boswellic acid) has also been extracted from the gum resin and stem bark of *Boswellia papyrifera* [199], *B. sacra* [200–202], and *B. serrata* [203,204]. Gum resin extracts of various *Boswellia* spp. have been reported to possess broadly effective antiviral activity [205,206]. 11-keto boswellic acid exhibits anti-inflammatory activity, inhibits 5-lipoxygenase with IC$_{50}$ values of 2.8 to 8.8 µM [207], downregulates TNF-α, and decreases the levels of the proinflammatory cytokines interleukin 1α (IL-1α), IL-2, IL-4, and IL-6 and interferon gamma (IFN-γ) [208,209]. EVD, however, is associated with an intense immune response that leads to the production of proinflammatory cytokines, thereby contributing to the pathogenesis of EVD by causing tissue damage and multiple organ failure [210–212]. Inhibiting the expression of proinflammatory cytokines could be a potential therapeutic strategy for EVD. 11-keto boswellic acid was also reported to inhibit prolyl endopeptidase (PEP) with an IC$_{50}$ of 36.32 µM [199].

Table 4. Names, PubChem IDs, 2D structures, and sources of the potential lead compounds. Marvin 23.3.0 by ChemAxon (https://www.chemaxon.com accessed 11th March, 2023) was used to generate the 2D structures.

Compound ID (PubChem Compound ID)	Common Name/IUPAC Name	Source/Origin	2D Structure
ZINC000034518176 (CID: 10836206)	(3S,4aR,6aR,6bS,8aR,11R,12S,12aS, 14aR,14bR)-4,4,6a,6b,8a,11,12,14b-octamethyl-2,3,4a,5,6,7,8,9,10,11,12,12a,14,14a-tetradecahydro-1H-picen-3-ol	*Vernonanthura chamaedrys* [187,188], *Mangifera indica* [189], *Cadia purpurea* [190], *Calendula officinalis* [191], *Pinalia leucantha* [192], *Ilex aquifolium* [193], *I. goshiensis* [194], and *Rhodomyrtus tomentosa* [195]	
ZINC000095485942 (CID: 163021364)	(1R,2R,4R,7S,8R,10R,11S,12S,13R,18R)-7-(furan-3-yl)-10,13-dihydroxy-8,12,17,17-tetramethyl-3,6,16-trioxapentacyclo[9.9.0.0^{2,4}.0^{2,8}.0^{12,18}]icosane-5,15,20-trione	-	
NANPDB2933 (CID: 102019659)	2-hydroxyseneganolide	*Khaya senegalensis* [179–181]	
ZINC000085531689 (CID: 97042015)	(4S,4aR,7S,7aR,12bR)-10-[(4S,4aS,7R,7aS,12bR)-7,9-dihydroxy-3-methyl-2,4,4a,7,7a,13-hexahydro-1H-4,12-methanobenzofuro[3,2-e]isoquinolin-10-yl]-3-methyl-2,4,4a,7,7a,13-hexahydro-1H-4,12-methanobenzofuro[3,2-e]isoquinoline-7,9-diol	-	
ZINC000014089759 (CID: 9847548)	11-keto boswellic acid	*Boswellia papyrifera* [199], *Boswellia sacra* [200–202], and *Boswellia serrata* [203,204]	
ZINC000085568136 (CID: Not available)	5-[(11R,12R,17R,18S)-12,22-dihydroxy-11-(4-hydroxy-3-methoxyphenyl)-4,10-dioxahexacyclo[15.7.1.0^{2,15}.0^{3,8}.0^{9,14}.0^{21,25}]pentacosa-1(25),2,8,14,19,21,23-heptaen-18-yl]-2H-indol-2-ylium	-	
ZINC000095912717 (CID: 12080815)	Lancifodilactone C	*Schisandra chinensis* (Turcz.) Baill [184] and *Schisandra lancifolia* [185]	

2.11. Limitations of the Study

A major drawback of this study is its lack of experimental testing of the identified compounds to validate their potential anti-VP40 and anti-EBOV activity. Without experimental validation, the effectiveness and safety of these compounds cannot be conclusively established, which limits their potential as viable drug candidates. Therefore, future research efforts should focus on experimental testing to assess the activity and safety of potential lead compounds. Another major caveat of this study concerns the predicted structures from I-TASSER, which was used for molecular docking and dynamics simulations. Since the flexible loop regions in VP40 found between residues 1–43 were not resolved in the parent template (PDB ID: 1ES6), the modeled structure may not accurately reflect the actual structure of VP40. However, the selected I-TASSER model had a C-score of −0.68 and an estimated TM-score of 0.63. I-TASSER-predicted models with TM scores >0.5 and C scores >−1.5 have been reported to have very good false positive and false negative rates of 0.05 and 0.09, respectively [41], implying that the selected structure could be reasonably accurate since it falls within this range. The success of computational drug discovery studies depends on the availability and quality of data. Subjecting the modelled structure to energy minimization and subsequent MD simulations could help fix the structures and provide a reasonably stable starting point for analysis. Furthermore, this study employed multiple robust computational approaches (including the validation of the molecular docking tool) to mitigate any potential errors that could have arisen.

3. Materials and Methods

Pharmacoinformatics-based techniques were employed to identify potential VP40 inhibitors from natural-product-derived compounds curated from African and Chinese sources (Figure 7) as performed in a previous study [213]. Approved drugs from various institutions were also obtained and screened (Figure 7). The study used structure-based virtual screening coupled with MD simulations and molecular mechanics Poisson–Boltzmann surface area (MM/PBSA) analyses to propose compounds with plausible binding affinity and mechanisms of binding. The shortlisted compounds were subjected to safety and toxicity profiling to further shortlist those with insignificant toxicity concerns. The biological activity and anti-EBOV activity of the shortlisted compounds were also determined.
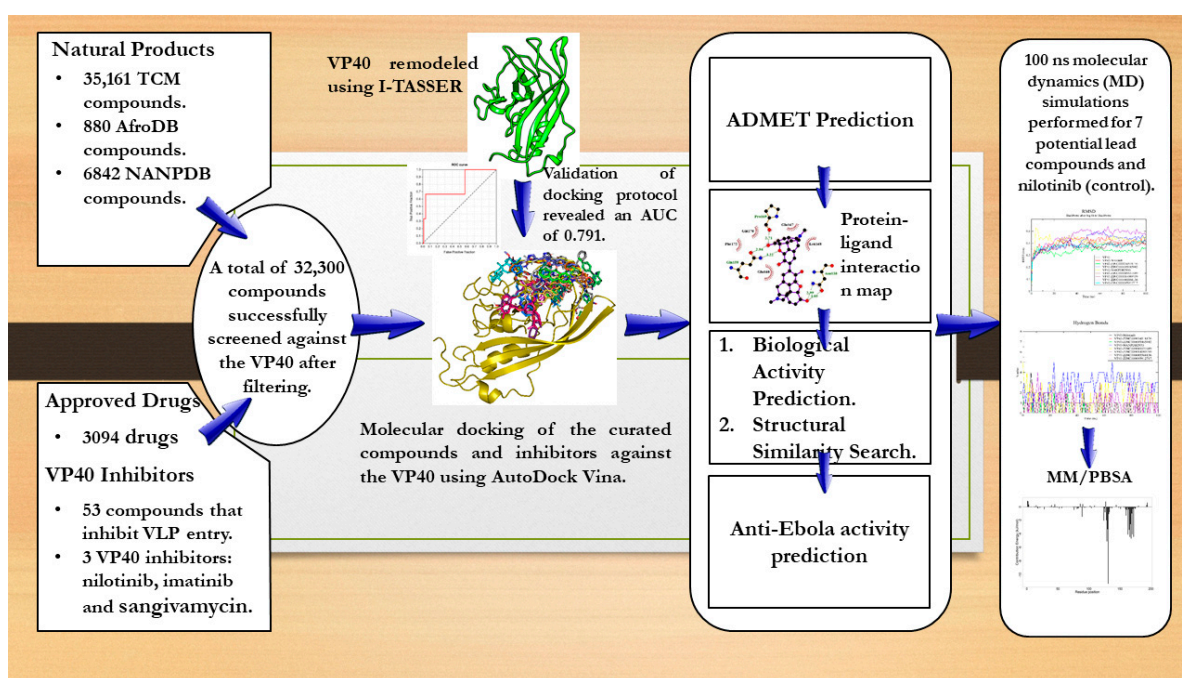
Figure 7. Schema of methodology detailing the step-by-step approach used to identify potential anti-VP40 compounds.

3.1. Target Retrieval and Preparation

Due to the critical role of the NTD of VP40 in oligomerization and VLP production, this study considered the NTD of the Ebola virus in molecular docking and dynamics simulations. The use of only the NTD did not negatively affect the study as the separation of the CTD from the NTD is required for VP40's transformation from its dimeric form to its hexameric form or octameric ring structure [214]. The crystal structures of the NTD of the matrix protein VP40 from Zaire Ebola virus with PDB IDs of 1H2C and 7K5L were obtained from the Protein Data Bank (PDB), a global resource that contains a wealth of three-dimensional (3D) information about experimentally determined biological macromolecules [35,215,216]. The 3D structures were visualized using PyMOL (version 2.5.2) [217–219]. Due to missing residues, the structure of the NTD of VP40 was remodeled using two different modelling techniques comprising I-TASSER [40–42,220] and Modeller (version 10.2) [221–223]. The sequence of the VP40 NTD was extracted from UniprotKB since both structures had missing residues. After careful examination of three Zaire EBOV sequences from UniprotKB with IDs of Q05128 (strain Mayinga-76), Q77DJ6 (strain Kikwit-95), and Q2PDK5 (strain Gabon-94), it was observed that all three strains had the same sequence. Using the 7K5L and 3TCQ models as templates, Modeller was employed to generate five structures. The sequence was also submitted to I-TASSER to predict reasonable structures for comparison. The best structure from each technique was selected based on the lowest discrete optimized potential energy (DOPE) score for Modeller and the highest confidence score for I-TASSER. Between the top 2 structures, the model with the most reasonable fold for the missing residues was selected for this study.

Prior to the molecular docking studies, the selected VP40 structure was energy-minimized using GROMACS 5.1.5 [224–226] in order to achieve a state of lower potential energy [227,228], thereby rendering the structure more stable. After energy minimization, the resulting structure was visualized in PyMOL, wherein the water molecules and ions were removed.

3.2. Binding Site Determination

Existing literature on Ebola VP40 was probed to identify previously determined active sites. The Computed Atlas of Surface Topography of proteins (CASTp) was also used to determine binding sites of the NTD of the VP40 protein [229–231].

3.3. Obtaining and Preparing Ligand Libraries

A total of 880 small molecules were retrieved from AfroDb, a library of natural compounds of African origin [232]. A total of 6842 compounds were also obtained in 2D spatial data file (sdf) format from the Northern African Natural Products Database (NANPDB) [233] and converted to 3D structures using Open Babel's "gen3d" option as previously described [213]. NANPDB is a repository of natural products from plant, animal, fungal, and bacterial sources that are available in Northern Africa [233]. A total of 35,161 compounds were also retrieved from the Traditional Chinese Medicine (TCM) database (TCM@Taiwan), a catalog of Zinc15 database [171,234]. Duplicates were removed from these libraries, and the natural products were then pre-filtered based on molecular weight (as described previously) [235]. Only compounds with molecular weights between 150 g/mol and 600 g/mol were used in this study. A total of 773, 3619, and 25,196 compounds from the AfroDb, NANPDB, and TCM libraries had molecular weights within the threshold and were used for this study.

Furthermore, 3D structures of 3094 approved drugs were obtained from Selleckchem Inc. (Houston, TX, USA) and included in the screening library. The approved drugs were curated from various institutions, including U.S. Food and Drug Administration (FDA, Silver Spring, MD, USA), China Food and Drug Administration (CFDA, Beijing, China), European Medicines Agency (EMA, Amsterdam, The Netherlands), Heads of Medicines Agency (HMA, Amsterdam, The Netherlands), and Pharmaceuticals and Medical Devices Agency (PMDA, Chiyoda-ku, Tokyo, Japan).

Literature search was conducted to identify experimentally tested VP40 inhibitors that could be used as standards in this study. Nilotinib and imatinib were shown to reduce the release of VLPs [82]. NP and VP40 levels were also observed to be lower in VLPs treated with nilotinib and imatinib at tested concentrations of 10 and 20 μM [82]. Using a VP40-based VLP assay to screen a library of compounds, sangivamycin (at concentrations of 37.5, 75, 150, and 300 nM) was reported to disrupt EBOV VP40 membrane localization and decrease VLP release; however, it did not affect VP40 abundance [236]. Another study also identified 53 compounds that inhibit entry of VLPs containing the GP and VP40 proteins fused with a beta-lactamase reporter protein [237]. However, the study also highlighted the possibility that some of the drugs were beta-lactamase inhibitors instead of VLP-entry inhibitors [237]. Herein, the 3D structures of these compounds were obtained from PubChem [172,238,239]. Compounds that had no 3D structures were ignored since converting them from 2D could introduce potential errors in their molecular descriptions, such as errors in connectivity, missing bonds, and abnormal geometries, which could influence their docking scores. Due to the uncertainty of whether all 53 compounds were specific Ebola VLP entry inhibitors [237], only nilotinib, imatinib, and sangivamycin were used as standards for this study [82,236]. However, the other inhibitors were also screened against VP40 to investigate their binding to this protein.

The small molecules in "sdf" formats were energy minimized using the universal force field (UFF) [240] via the OpenBabel option in PyRx [241,242]. The compounds were then converted to AutoDock Vina's compatible "Protein Data Bank, Partial Charge (Q), & Atom Type (T)" (PDBQT) format.

3.4. Docking Validation

Prior to the molecular-docking procedure, the ability of AutoDock Vina to discriminate between anti-VP40 actives and inactives was validated using Screening Explorer [59]. The three known inhibitors, comprising nilotinib, imatinib, and sangivamycin, were used to generate 150 decoys (50 each) via Database of Useful Decoys: Enhanced (DUD-E) [243]. The three known inhibitors and the 150 decoys were screened against the VP40 protein, and the results were uploaded to Screening Explorer to compute the area under the receiver operating characteristics curve (ROC AUC), Boltzmann-enhanced discrimination of receiver operating characteristics (BEDROC), total gain (TG), and the robustness initial enhancement (RIE).

3.5. Molecular Docking

Virtual screening is a substantive computational approach of tremendous importance in in silico drug design that employs computer-based methods to discover ligands that can bind a protein based on biological structures [244,245]. In this study, AutoDock Vina embedded in PyRx (version 0.9.2) was used to perform molecular-docking processes [242,246]. The grid box was defined to cover the RNA binding site and the loop region with dimensions of (39.05 × 32.15 × 33.42) Å^3 and centered at 30.17, 27.82, and 38.36 Å. An exhaustiveness value of eight was also set for the docking run. After docking, the ligands were ranked in descending order based on their docking scores. A good docking score does not imply a strong binding affinity as previous studies have shown that docking scores are not reliable in terms of ranking the binding potency of compounds [247–249]. Nevertheless, molecular docking has been shown to reasonably generate conformations that are similar to experimentally determined protein–ligand complex structures [247,248]. Thus, a good docking score provides a conformation/pose, which can be used as a good starting point for MD simulation-based analyses [247]. Herein, compounds with docking scores lower than that of the best-performing inhibitor were shortlisted for further analysis.

3.6. Pharmacological and Toxicity Profiling of Molecules

The drug likeness of the shortlisted compounds was assessed using Lipinski's rule of 5 and Veber's rule. ADMET properties usually depend on the molecular descriptors of the

compound. The possibility for the in silico prediction of these properties for new structures allows one to considerably accelerate drug design and optimization to increase efficiency. ADMET constitutes the structural, physiochemical, biochemical, and pharmacokinetic properties of a drug molecule as well as its toxicity, which are essential for evaluating its pharmacodynamics. The interactions of the structural properties of a compound with its physical environment can govern its physiochemical properties (e.g., solubility, lipophilicity, stability, etc.), while interactions with proteins are important determinants of its biochemical properties (e.g., metabolism). At the highest level, when these physicochemical and biochemical properties interact with living systems, they confer pharmacokinetic effects and toxicity [250]. The pharmacological properties of the compounds were evaluated using SwissADME [251]. DataWarrior 5.5.0 was also used to predict the toxicity risks of the shortlisted compounds [89].

3.7. Protein–Ligand Interaction

In addition to the binding affinity of the molecules, the inhibitory effect of compounds can be determined by analyzing their interactions with receptor molecules. In particular, multiple hydrogen bond interactions ensure the stability of drug–receptor complexes and may influence the activity of the drug [163]. LigPlot$^+$ (v1.4.5) and PyMOL were used to visualize the binding interactions between the VP40 and the top compounds.

3.8. Prediction of Biological Activities of Lead Compounds

The biological activities of the identified lead compounds were predicted using prediction of activity spectra for substances (PASS) [90]. In this method, prediction is based on an analysis of the structure–activity relationships in the training set containing information on the structure and biological activity of more than 300,000 compounds. PASS may be used to find new targets for known pharmaceuticals or for searching for new biologically active substances. Compounds in the Simplified Molecular Input Line Entry System (SMILES) format were used as inputs. In addition, anti-Ebola, a regression-based algorithm, was employed to predict the potential EBOV-inhibitory activities of the selected compounds using their SDF formats. Anti-Ebola predicts the inhibition efficiency of compounds using quantitative structure–activity relationship (QSAR) information of molecules that have experimentally tested anti-Ebola activities [94]. The random forest (RF) and support vector machine (SVM) algorithms of Anti-Ebola were employed for the activity predictions conducted in this study [94].

3.9. MD Simulations of VP40 and VP40–Ligand Complexes

MD simulations were performed on the unbound VP40 and VP40–ligand complexes using GROMACS 5.1.5 [224]. Ligand topologies were generated using LigParGen [252]. The all-atom optimized potentials for liquid simulations (OPLS/AA) force field was used to prepare the topology of the VP40 protein [253,254]. Each system was solvated in a cubically shaped box and neutralized by the addition of chlorine or sodium ions depending on the system's charge. Energy minimization was performed for each system for 1000 steps using the steepest descent algorithm and then further equilibrated to restrain and relax protein and ligand positions. Finally, an MD simulation of the complexes was performed for 100 ns, and Qtgrace was used to plot all graphs generated from the MD simulations [255].

3.10. Evaluation of Lead Compounds Using MM/PBSA

MM/PBSA calculations were performed for the VP40–ligand complexes after the 100 ns MD simulation using g_mmpbsa [164]. The *van der Waals* (vdW), electrostatic, polar solvation, solvent-accessible surface area (SASA), and binding free energies of each complex were computed. The per-residue energy contributions of each complex were also determined to evaluate the critical residues favoring or preventing ligand binding. The R programming package was used to plot the graphs of free binding energy.

4. Conclusions

Over the years, computer-aided drug design (CADD) techniques have proven to be advantageous for the discovery of effective treatments for different diseases. Therefore, this study employed similar techniques to identify potential anti-EBOV VP40 lead compounds from natural product sources and to repurpose currently approved drugs. This study bolsters the findings of existing studies undertaken to find potential EBOV inhibitors to increase our therapeutic arsenal against EVD [94,237,256–258]. A total of 32,300 ligands were successfully screened against VP40, of which 65 (42 natural products and 23 approved drugs) were predicted to be potential anti-EBOV compounds. The potential lead compounds demonstrated better docking scores with respect to VP40 (−8 to −9.1 kcal/mol) than the three known inhibitors (nilotinib, imatinib, and sangivamycin) used (−6.3 to −7.9 kcal/mol). MD simulations and MM/PBSA computations also showed that the potential lead compounds had stronger binding affinity to VP40 (−46.97 to −118.9 kJ/mol) than nilotinib (−11.21 kJ/mol), which was used as a control. The in silico characterization of the potential lead compounds using ADMET testing corroborated their drug-like properties. It was observed that most of the compounds bind in the loop region rather than the RNA binding site as suggested previously [48]. The biological activities of the lead compounds that were predicted using PASS suggest that these lead compounds possess potential antiviral mechanisms of action for inhibiting viral replication and budding. The promising potential lead compounds identified herein have the propensity to act as anti-Ebola VP40 scaffolds. The results obtained indicate that these compounds deserve to be experimentally tested in vitro and in vivo to ascertain their ability to combat the infection and spread of EVD.

References

1. Koch, L.K.; Cunze, S.; Kochmann, J.; Klimpel, S. Bats as putative Zaire ebolavirus reservoir hosts and their habitat suitability in Africa. *Sci. Rep.* **2020**, *10*, 14268. [CrossRef] [PubMed]
2. Eloy, P.; Laouénan, C.; Beavogui, A.H.; Keita, S.; Manchon, P.; Etard, J.-F.; Sissoko, D.; Mentré, F.; Malvy, D. High doses of favipiravir in two men survivors of Ebola virus disease carrying Ebola virus in semen in Guinea. *Idcases* **2022**, *27*, e01412. [CrossRef] [PubMed]
3. Purpura, L.J.; Rogers, E.; Baller, A.; White, S.; Soka, M.; Choi, M.J.; Mahmoud, N.; Wasunna, C.; Massaquoi, M.; Kollie, J.; et al. Ebola Virus RNA in Semen from an HIV-Positive Survivor of Ebola. *Emerg. Infect. Dis.* **2017**, *23*, 714–715. [CrossRef] [PubMed]
4. Uyeki, T.M.; Erickson, B.R.; Brown, S.; McElroy, A.; Cannon, D.; Gibbons, A.; Sealy, T.; Kainulainen, M.H.; Schuh, A.J.; Kraft, C.S.; et al. Ebola Virus Persistence in Semen of Male Survivors. *Clin. Infect. Dis.* **2016**, *62*, 1552–1555. [CrossRef]
5. Deen, G.F.; Broutet, N.; Xu, W.; Knust, B.; Sesay, F.R.; McDonald, S.L.; Ervin, E.; Marrinan, J.E.; Gaillard, P.; Habib, N.; et al. Ebola RNA Persistence in Semen of Ebola Virus Disease Survivors—Final Report. *N. Engl. J. Med.* **2017**, *377*, 1428–1437. [CrossRef]
6. Fischer, R.J.; Judson, S.; Miazgowicz, K.; Bushmaker, T.; Munster, V.J. Ebola Virus Persistence in Semen Ex Vivo. *Emerg. Infect. Dis.* **2016**, *22*, 289–291. [CrossRef]
7. Jacob, S.T.; Crozier, I.; Fischer, W.A., 2nd; Hewlett, A.; Kraft, C.S.; Vega, M.A.; Soka, M.J.; Wahl, V.; Griffiths, A.; Bollinger, L.; et al. Ebola virus disease. *Nat. Rev. Dis. Prim.* **2020**, *6*, 13. [CrossRef]
8. Geisbert, T.W.; Jahrling, P.B. Differentiation of filoviruses by electron microscopy. *Virus Res.* **1995**, *39*, 129–150. [CrossRef]

9.   Karthick, V.; Nagasundaram, N.; Doss, C.G.P.; Chakraborty, C.; Siva, R.; Lu, A.; Zhang, G.; Zhu, H. Virtual screening of the inhibitors targeting at the viral protein 40 of Ebola virus. *Infect. Dis. Poverty* **2016**, *5*, 12. [CrossRef]

10. Aleksandrowicz, P.; Marzi, A.; Biedenkopf, N.; Beimforde, N.; Becker, S.; Hoenen, T.; Feldmann, H.; Schnittler, H.-J. Ebola Virus Enters Host Cells by Macropinocytosis and Clathrin-Mediated Endocytosis. *J. Infect. Dis.* **2011**, *204*, S957–S967. [CrossRef]

11. Bharat, T.A.; Noda, T.; Riches, J.D.; Kraehling, V.; Kolesnikova, L.; Becker, S.; Kawaoka, Y.; Briggs, J.A. Structural dissection of Ebola virus and its assembly determinants using cryo-electron tomography. *Proc. Natl. Acad. Sci. USA* **2012**, *109*, 4275–4280. [CrossRef]

12. Billioux, B.J.; Smith, B.; Nath, A. Neurological Complications of Ebola Virus Infection. *Neurotherapeutics* **2016**, *13*, 461–470. [CrossRef]

13. MacDermott, N.; Herberg, J. Ebola: Lessons learned. *Paediatr. Child Health* **2016**, *27*, 128–134. [CrossRef]

14. Johnson, R.F.; McCarthy, S.E.; Godlewski, P.J.; Harty, R.N. Ebola Virus VP35-VP40 Interaction Is Sufficient for Packaging 3E-5E Minigenome RNA into Virus-Like Particles. *J. Virol.* **2006**, *80*, 5135–5144. [CrossRef]

15. Timmins, J.; Scianimanico, S.; Schoehn, G.; Weissenhorn, W. Vesicular Release of Ebola Virus Matrix Protein VP40. *Virology* **2001**, *283*, 1–6. [CrossRef] [PubMed]

16. Adu-Gyamfi, E.; Digman, M.A.; Gratton, E.; Stahelin, R.V. Investigation of Ebola VP40 Assembly and Oligomerization in Live Cells Using Number and Brightness Analysis. *Biophys. J.* **2012**, *102*, 2517–2525. [CrossRef]

17. Stahelin, R.V. Membrane binding and bending in Ebola VP40 assembly and egress. *Front. Microbiol.* **2014**, *5*, 300. [CrossRef]

18. Noda, T.; Sagara, H.; Suzuki, E.; Takada, A.; Kida, H.; Kawaoka, Y. Ebola Virus VP40 Drives the Formation of Virus-Like Filamentous Particles Along with GP. *J. Virol.* **2002**, *76*, 4855–4865. [CrossRef] [PubMed]

19. Bornholdt, Z.A.; Noda, T.; Abelson, D.M.; Halfmann, P.; Wood, M.R.; Kawaoka, Y.; Saphire, E.O. Structural Rearrangement of Ebola Virus VP40 Begets Multiple Functions in the Virus Life Cycle. *Cell* **2013**, *154*, 763–774. [CrossRef]

20. Gomis-Ruth, F.X.; Dessen, A.; Timmins, J.; Bracher, A.; Kolesnikowa, L.; Becker, S.; Klenk, H.-D.; Weissenhorn, W. The Matrix Protein VP40 from Ebola Virus Octamerizes into Pore-like Structures with Specific RNA Binding Properties. *Structure* **2003**, *11*, 423–433. [CrossRef] [PubMed]

21. Saxena, D.; Kaul, G.; Dasgupta, A.; Chopra, S. Atoltivimab/maftivimab/odesivimab (Inmazeb) combination to treat infection caused by Zaire ebolavirus. *Drugs Today* **2021**, *57*, 483. [CrossRef]

22. Markham, A. REGN-EB3: First Approval. *Drugs* **2021**, *81*, 175–178. [CrossRef] [PubMed]

23. Hansen, F.; Feldmann, H.; Jarvis, M.A. Targeting Ebola virus replication through pharmaceutical intervention. *Expert Opin. Investig. Drugs* **2021**, *30*, 201–226. [CrossRef]

24. Lee, A. Ansuvimab: First Approval. *Drugs* **2021**, *81*, 595–598. [CrossRef]

25. Aschenbrenner, D.S. Monoclonal Antibody Approved to Treat Ebola. *AJN Am. J. Nurs.* **2021**, *121*, 22. [CrossRef] [PubMed]

26. Ngo, H.X.; Garneau-Tsodikova, S. What are the drugs of the future? *MedChemComm* **2018**, *9*, 757–758. [CrossRef] [PubMed]

27. Iversen, P.L.; Kane, C.D.; Zeng, X.; Panchal, R.G.; Warren, T.K.; Radoshitzky, S.R.; Kuhn, J.H.; Mudhasani, R.R.; Cooper, C.L.; Shurtleff, A.C.; et al. Recent successes in therapeutics for Ebola virus disease: No time for complacency. *Lancet Infect. Dis.* **2020**, *20*, e231–e237. [CrossRef]

28. Krishnasamy, L.; Saikumar, C. Updates on Treatment of Ebola Virus Disease. *Malays. J. Med. Sci.* **2015**, *22*, 54–57.

29. Thi, E.P.; Mire, C.E.; Lee, A.C.H.; Geisbert, J.B.; Zhou, J.Z.; Agans, K.N.; Snead, N.M.; Deer, D.J.; Barnard, T.R.; Fenton, K.A.; et al. Lipid nanoparticle siRNA treatment of Ebola-virus-Makona-infected nonhuman primates. *Nature* **2015**, *521*, 362–365. [CrossRef]

30. Taylor, R.; Kotian, P.; Warren, T.; Panchal, R.; Bavari, S.; Julander, J.; Dobo, S.; Rose, A.; El-Kattan, Y.; Taubenheim, B.; et al. BCX4430—A broad-spectrum antiviral adenosine nucleoside analog under development for the treatment of Ebola virus disease. *J. Infect. Public Health* **2016**, *9*, 220–226. [CrossRef]

31. Warren, T.K.; Wells, J.; Panchal, R.G.; Stuthman, K.S.; Garza, N.L.; Van Tongeren, S.A.; Dong, L.; Retterer, C.J.; Eaton, B.P.; Pegoraro, G.; et al. Protection against filovirus diseases by a novel broad-spectrum nucleoside analogue BCX4430. *Nature* **2014**, *508*, 402–405. [CrossRef] [PubMed]

32. Furuta, Y.; Takahashi, K.; Fukuda, Y.; Kuno, M.; Kamiyama, T.; Kozaki, K.; Nomura, N.; Egawa, H.; Minami, S.; Watanabe, Y.; et al. In Vitro and In Vivo Activities of Anti-Influenza Virus Compound T-705. *Antimicrob. Agents Chemother.* **2002**, *46*, 977–981. [CrossRef] [PubMed]

33. Spurgers, K.B.; Sharkey, C.M.; Warfield, K.L.; Bavari, S. Oligonucleotide antiviral therapeutics: Antisense and RNA interference for highly pathogenic RNA viruses. *Antivir. Res.* **2008**, *78*, 26–36. [CrossRef]

34. Xie, T.; Song, S.; Li, S.; Ouyang, L.; Xia, L.; Huang, J. Review of natural product databases. *Cell Prolif.* **2015**, *48*, 398–404. [CrossRef]

35. Rose, P.W.; Prlić, A.; Altunkaya, A.; Bi, C.; Bradley, A.R.; Christie, C.H.; Di Costanzo, L.; Duarte, J.M.; Dutta, S.; Feng, Z.; et al. The RCSB protein data bank: Integrative view of protein, gene and 3D structural information. *Nucleic Acids Res.* **2016**, *45*, D271–D281. [CrossRef]

36. Burley, S.K.; Bhikadiya, C.; Bi, C.; Bittrich, S.; Chen, L.; Crichlow, G.V.; Christie, C.H.; Dalenberg, K.; Di Costanzo, L.; Duarte, J.M.; et al. RCSB Protein Data Bank: Powerful new tools for exploring 3D structures of biological macromolecules for basic and applied research and education in fundamental biology, biomedicine, biotechnology, bioengineering and energy sciences. *Nucleic Acids Res.* **2020**, *49*, D437–D451. [CrossRef] [PubMed]

37. Berman, H.M.; Westbrook, J.; Feng, Z.; Gilliland, G.; Bhat, T.N.; Weissig, H.; Shindyalov, I.N.; Bourne, P.E. The Protein Data Bank. *Nucleic Acids Res.* **2000**, *28*, 235–242. [CrossRef] [PubMed]

38. Landeras-Bueno, S.; Wasserman, H.; Oliveira, G.; VanAernum, Z.L.; Busch, F.; Salie, Z.L.; Wysocki, V.H.; Andersen, K.; Saphire, E.O. Cellular mRNA triggers structural transformation of Ebola virus matrix protein VP40 to its essential regulatory form. *Cell Rep.* **2021**, *35*, 108986. [CrossRef]

39. Khan, S.; Fakhar, Z.; Ahmad, A. Targeting ebola virus VP40 protein through novel inhibitors: Exploring the structural and dynamic perspectives on molecular landscapes. *J. Mol. Model.* **2021**, *27*, 49. [CrossRef] [PubMed]

40. Yang, J.; Zhang, Y. I-TASSER server: New development for protein structure and function predictions. *Nucleic Acids Res.* **2015**, *43*, W174–W181. [CrossRef]

41. Zhang, Y. I-TASSER server for protein 3D structure prediction. *BMC Bioinform.* **2008**, *9*, 40. [CrossRef] [PubMed]

42. Roy, A.; Kucukural, A.; Zhang, Y. I-TASSER: A unified platform for automated protein structure and function prediction. *Nat. Protoc.* **2010**, *5*, 725–738. [CrossRef] [PubMed]

43. Dessen, A.; Volchkov, V.; Dolnik, O.; Klenk, H.; Weissenhorn, W. Crystal structure of the matrix protein VP40 from Ebola virus. *EMBO J.* **2000**, *19*, 4228–4236. [CrossRef]

44. Tsai, H.-H.; Tsai, C.-J.; Ma, B.; Nussinov, R. In silico protein design by combinatorial assembly of protein building blocks. *Protein Sci.* **2009**, *13*, 2753–2765. [CrossRef]

45. Pettersen, E.F.; Goddard, T.D.; Huang, C.C.; Couch, G.S.; Greenblatt, D.M.; Meng, E.C.; Ferrin, T.E. UCSF Chimera?A visualization system for exploratory research and analysis. *J. Comput. Chem.* **2004**, *25*, 1605–1612. [CrossRef]

46. Adu-Gyamfi, E.; Soni, S.P.; Jee, C.S.; Digman, M.A.; Gratton, E.; Stahelin, R.V. A Loop Region in the N-Terminal Domain of Ebola Virus VP40 Is Important in Viral Assembly, Budding, and Egress. *Viruses* **2014**, *6*, 3837–3854. [CrossRef] [PubMed]

47. Odhar, H.A.; Rayshan, A.M.; Ahjel, S.W.; Hashim, A.A.; Albeer, A.A.M.A. Molecular docking enabled updated screening of the matrix protein VP40 from Ebola virus with millions of compounds in the MCULE database for potential inhibitors. *Bioinformation* **2019**, *15*, 627–632. [CrossRef] [PubMed]

48. Nasution, M.A.F.; Alkaff, A.H.; Tambunan, U.S.F. Discovery of Indonesian natural products as potential inhibitor of Ebola virus VP40 through molecular docking simulation. *AIP Conf. Proc.* **2018**, *2023*, 020055. [CrossRef]

49. Licata, J.M.; Simpson-Holley, M.; Wright, N.T.; Han, Z.; Paragas, J.; Harty, R.N. Overlapping Motifs (PTAP and PPEY) within the Ebola Virus VP40 Protein Function Independently as Late Budding Domains: Involvement of Host Proteins TSG101 and VPS-4. *J. Virol.* **2003**, *77*, 1812–1819. [CrossRef]

50. Han, Z.; Ruthel, G.; Dash, S.; Berry, C.T.; Freedman, B.D.; Harty, R.N.; Shtanko, O. Angiomotin regulates budding and spread of Ebola virus. *J. Biol. Chem.* **2020**, *295*, 8596–8601. [CrossRef]

51. Yasuda, J.; Nakao, M.; Kawaoka, Y.; Shida, H. Nedd4 Regulates Egress of Ebola Virus-Like Particles from Host Cells. *J. Virol.* **2003**, *77*, 9987–9992. [CrossRef]

52. Han, Z.; Lu, J.; Liu, Y.; Davis, B.; Lee, M.S.; Olson, M.A.; Ruthel, G.; Freedman, B.D.; Schnell, M.J.; Wrobel, J.E.; et al. Small-Molecule Probes Targeting the Viral PPxY-Host Nedd4 Interface Block Egress of a Broad Range of RNA Viruses. *J. Virol.* **2014**, *88*, 7294–7306. [CrossRef] [PubMed]

53. Iglesias-Bexiga, M.; Palencia, A.; Corbi-Verge, C.; Martin-Malpartida, P.; Blanco, F.J.; Macias, M.J.; Cobos, E.S.; Luque, I. Binding site plasticity in viral PPxY Late domain recognition by the third WW domain of human NEDD4. *Sci. Rep.* **2019**, *9*, 15076. [CrossRef]

54. Johnson, K.A.; Pokhrel, R.; Budicini, M.R.; Gerstman, B.S.; Chapagain, P.P.; Stahelin, R.V. A Conserved Tryptophan in the Ebola Virus Matrix Protein C-Terminal Domain Is Required for Efficient Virus-Like Particle Formation. *Pathogens* **2020**, *9*, 402. [CrossRef]

55. Chukwuemeka, P.O.; Umar, H.I.; Iwaloye, O.; Oretade, O.M.; Olowosoke, C.B.; Elabiyi, M.O.; Igbe, F.O.; Oretade, O.J.; Eigbe, J.O.; Adeojo, F.J. Targeting p53-MDM2 interactions to identify small molecule inhibitors for cancer therapy: Beyond "Failure to rescue". *J. Biomol. Struct. Dyn.* **2021**, *40*, 9158–9176. [CrossRef] [PubMed]

56. Dankwa, B.; Broni, E.; Enninful, K.S.; Kwofie, S.K.; Wilson, M.D. Consensus docking and MM-PBSA computations identify putative furin protease inhibitors for developing potential therapeutics against COVID-19. *Struct. Chem.* **2022**, *33*, 2221–2241. [CrossRef] [PubMed]

57. Cleves, M.A. Comparative Assessment of Three Common Algorithms for Estimating the Variance of the Area under the Nonparametric Receiver Operating Characteristic Curve. *Stata J.* **2002**, *2*, 280–289. [CrossRef]

58. Sun, X.; Xu, W. Fast Implementation of DeLong's Algorithm for Comparing the Areas Under Correlated Receiver Operating Characteristic Curves. *IEEE Signal Process. Lett.* **2014**, *21*, 1389–1393. [CrossRef]

59. Empereur-Mot, C.; Zagury, J.-F.; Montes, M. Screening Explorer–An Interactive Tool for the Analysis of Screening Results. *J. Chem. Inf. Model.* **2016**, *56*, 2281–2286. [CrossRef] [PubMed]

60. Doan, H.T.T.; Noh, J.H.; Kim, Y.H.; Yoo, M.S.; Reddy, K.E.; Jung, S.C.; Kang, S.W. The efficacy of avermectins (ivermectin, doramectin and abamectin) as treatments for infestation with the tick Haemaphysalis longicornis on rabbits in Korea. *Vet. Parasitol.* **2013**, *198*, 406–409. [CrossRef]

61. Pereira, J.R. The efficiency of avermectins (abamectin, doramectin and ivermectin) in the control of Boophilus microplus, in artificially infested bovines kept in field conditions. *Vet. Parasitol.* **2009**, *162*, 116–119. [CrossRef]

62. Varghese, F.S.; Kaukinen, P.; Gläsker, S.; Bespalov, M.; Hanski, L.; Wennerberg, K.; Kümmerer, B.M.; Ahola, T. Discovery of berberine, abamectin and ivermectin as antivirals against chikungunya and other alphaviruses. *Antivir. Res.* **2016**, *126*, 117–124. [CrossRef]

63. Caly, L.; Druce, J.D.; Catton, M.G.; Jans, D.A.; Wagstaff, K.M. The FDA-approved drug ivermectin inhibits the replication of SARS-CoV-2 in vitro. *Antivir. Res.* **2020**, *178*, 104787. [CrossRef]

64. Heidary, F.; Gharebaghi, R. Ivermectin: A systematic review from antiviral effects to COVID-19 complementary regimen. *J. Antibiot.* **2020**, *73*, 593–602. [CrossRef] [PubMed]

65. Xu, T.-L.; Han, Y.; Liu, W.; Pang, X.-Y.; Zheng, B.; Zhang, Y.; Zhou, X.-N. Antivirus effectiveness of ivermectin on dengue virus type 2 in Aedes albopictus. *PLoS Negl. Trop. Dis.* **2018**, *12*, e0006934. [CrossRef]

66. Afzal, S.; Raza, S.; Rabbani, M.; Firyal, S.; Altaf, I.; Naeem, Z. Antiviral Potential of Ivermectin against Peste des Petits Ruminants Virus (PPRV). *Pak. J. Zool.* **2021**, *53*, 1575–1578. [CrossRef]

67. Kinobe, R.T.; Owens, L. A systematic review of experimental evidence for antiviral effects of ivermectin and an in silico analysis of ivermectin's possible mode of action against SARS-CoV-2. *Fundam. Clin. Pharmacol.* **2021**, *35*, 260–276. [CrossRef]

68. Basler, C.F. Molecular pathogenesis of viral hemorrhagic fever. *Semin. Immunopathol.* **2017**, *39*, 551–561. [CrossRef] [PubMed]

69. Kesel, A.J. A system of protein target sequences for anti-RNA-viral chemotherapy by a vitamin B6-Derived zinc-Chelating trioxa-adamantane-triol. *Bioorganic Med. Chem.* **2003**, *11*, 4599–4613. [CrossRef] [PubMed]

70. Afanasieva, T.A.; Wahl-Jensen, V.; Seebach, J.; Schillers, H.; Nikova, D.; Ströher, U.; Feldmann, H.; Schnittler, H.-J. Hemor-rhagic Fevers: Endothelial Cells and Ebola-Virus Hemorrhagic Fever. In *Endothelial Biomedicine*; Cambridge University Press: Cambridge, UK, 2007; pp. 1311–1319, ISBN 9780511546198.

71. Geddawy, A.; Ibrahim, Y.F.; Elbahie, N.M.; Ibrahim, M.A. Direct acting anti-hepatitis C virus drugs: Clinical pharmacology and future direction. *J. Transl. Intern. Med.* **2017**, *5*, 8–17. [CrossRef]

72. Vallet-Pichard, A.; Pol, S. Grazoprevir/elbasvir combination therapy for HCV infection. *Ther. Adv. Gastroenterol.* **2016**, *10*, 155–167. [CrossRef]

73. Ng, T.I.; Tripathi, R.; Reisch, T.; Lu, L.; Middleton, T.; Hopkins, T.A.; Pithawalla, R.; Irvin, M.; Dekhtyar, T.; Krishnan, P.; et al. In Vitro Antiviral Activity and Resistance Profile of the Next-Generation Hepatitis C Virus NS3/4A Protease Inhibitor Glecaprevir. *Antimicrob. Agents Chemother.* **2018**, *62*, e01620-17. [CrossRef] [PubMed]

74. Cotter, T.G.; Jensen, D.M. Glecaprevir/pibrentasvir for the treatment of chronic hepatitis C: Design, development, and place in therapy. *Drug Des. Dev. Ther.* **2019**, *ume13*, 2565–2577. [CrossRef] [PubMed]

75. Lamb, Y.N. Glecaprevir/Pibrentasvir: First Global Approval. *Drugs* **2017**, *77*, 1797–1804. [CrossRef] [PubMed]

76. Pollyea, D.A.; Amaya, M.; Strati, P.; Konopleva, M.Y. Venetoclax for AML: Changing the treatment paradigm. *Blood Adv.* **2019**, *3*, 4326–4335. [CrossRef] [PubMed]

77. Cang, S.; Iragavarapu, C.; Savooji, J.; Song, Y.; Liu, D. ABT-199 (venetoclax) and BCL-2 inhibitors in clinical development. *J. Hematol. Oncol.* **2015**, *8*, 129. [CrossRef] [PubMed]

78. Seymour, J.F.; Kipps, T.J.; Eichhorst, B.; Hillmen, P.; D'Rozario, J.; Assouline, S.; Owen, C.; Gerecitano, J.; Robak, T.; De la Serna, J.; et al. Venetoclax–Rituximab in Relapsed or Refractory Chronic Lymphocytic Leukemia. *N. Engl. J. Med.* **2018**, *378*, 1107–1120. [CrossRef] [PubMed]

79. Korycka-Wolowiec, A.; Wolowiec, D.; Kubiak-Mlonka, A.; Robak, T. Venetoclax in the treatment of chronic lymphocytic leukemia. *Expert Opin. Drug Metab. Toxicol.* **2019**, *15*, 353–366. [CrossRef] [PubMed]

80. Alto, A.; Natesampillai, S.; Chandrasekar, A.P.; Krogman, A.; Misra, A.; Shweta, F.; VanLith, C.; Yao, J.D.; Cummins, N.W.; Badley, A.D. The Combination of Venetoclax and Ixazomib Selectively and Efficiently Kills HIV-Infected Cell Lines but Has Unacceptable Toxicity in Primary Cell Models. *J. Virol.* **2021**, *95*, e00138-21. [CrossRef]

81. Whitmer, S.L.; Ladner, J.T.; Wiley, M.; Patel, K.; Dudas, G.; Rambaut, A.; Sahr, F.; Prieto, K.; Shepard, S.S.; Carmody, E.; et al. Active Ebola Virus Replication and Heterogeneous Evolutionary Rates in EVD Survivors. *Cell Rep.* **2018**, *22*, 1159–1168. [CrossRef]

82. García, M.; Cooper, A.; Shi, W.; Bornmann, W.; Carrion, R.; Kalman, D.; Nabel, G.J. Productive Replication of Ebola Virus Is Regulated by the c-Abl1 Tyrosine Kinase. *Sci. Transl. Med.* **2012**, *4*, 123ra24. [CrossRef] [PubMed]

83. Capuzzi, S.J.; Sun, W.; Muratov, E.N.; Martínez-Romero, C.; He, S.; Zhu, W.; Li, H.; Tawa, G.; Fisher, E.G.; Xu, M.; et al. Computer-Aided Discovery and Characterization of Novel Ebola Virus Inhibitors. *J. Med. Chem.* **2018**, *61*, 3582–3594. [CrossRef]

84. Lipinski, C.A.; Lombardo, F.; Dominy, B.W.; Feeney, P.J. Experimental and computational approaches to estimate solubility and permeability in drug discovery and development settings. *Adv. Drug Deliv. Rev.* **2001**, *46*, 3–26. [CrossRef]

85. Barret, R. *Medicinal Chemistry*; Elsevier: Amsterdam, The Netherlands, 2018; pp. 97–100. ISBN 978-1-78548-288-5. [CrossRef]

86. Lipinski, C.A. Drug-like properties and the causes of poor solubility and poor permeability. *J. Pharmacol. Toxicol. Methods* **2000**, *44*, 235–249. [CrossRef] [PubMed]

87. Lipinski, C.A. Lead- and drug-like compounds: The rule-of-five revolution. *Drug Discov. Today Technol.* **2004**, *1*, 337–341. [CrossRef]

88. Veber, D.F.; Johnson, S.R.; Cheng, H.-Y.; Smith, B.R.; Ward, K.W.; Kopple, K.D. Molecular Properties That Influence the Oral Bioavailability of Drug Candidates. *J. Med. Chem.* **2002**, *45*, 2615–2623. [CrossRef] [PubMed]

89. Sander, T.; Freyss, J.; Von Korff, M.; Rufener, C. DataWarrior: An open-source program for chemistry aware data visualization and analysis. *J. Chem. Inf. Model.* **2015**, *55*, 460–473. [CrossRef]

90. Poroikov, V.V.; Filimonov, D.A.; Ihlenfeldt, W.-D.; Gloriozova, T.A.; Lagunin, A.A.; Borodina, Y.V.; Stepanchikova, A.V.; Nicklaus, M.C. PASS Biological Activity Spectrum Predictions in the Enhanced Open NCI Database Browser. *J. Chem. Inf. Comput. Sci.* **2003**, *43*, 228–236. [CrossRef]

91. Parasuraman, S. Prediction of activity spectra for substances. *J. Pharmacol. Pharmacother.* **2011**, *2*, 52–53. [CrossRef]

92. Filimonov, D.; Lagunin, A.A.; Gloriozova, T.A.; Rudik, A.; Druzhilovskii, D.S.; Pogodin, P.V.; Poroikov, V.V. Prediction of the Biological Activity Spectra of Organic Compounds Using the Pass Online Web Resource. *Chem. Heterocycl. Compd.* **2014**, *50*, 444–457. [CrossRef]

93. Lagunin, A.; Stepanchikova, A.; Filimonov, D.; Poroikov, V. PASS: Prediction of activity spectra for biologically active substances. *Bioinformatics* **2000**, *16*, 747–748. [CrossRef] [PubMed]

94. Rajput, A.; Kumar, M. Anti-Ebola: An initiative to predict Ebola virus inhibitors through machine learning. *Mol. Divers.* **2021**, *26*, 1635–1644. [CrossRef] [PubMed]

95. Plech, T.; Kaproń, B.; Łuszczki, J.J.; Wujec, M.; Paneth, A.; Siwek, A.; Kolaczkowski, M.; Żołnierek, M.; Nowak, G. Studies on the Anticonvulsant Activity and Influence on GABA-ergic Neurotransmission of 1,2,4-Triazole-3-thione- Based Compounds. *Molecules* **2014**, *19*, 11279–11299. [CrossRef]

96. Torres-García, I.; López-Martínez, J.L.; Muñoz-Dorado, M.; Rodríguez-García, I.; Álvarez-Corral, M. Marine Terpenic Endoperoxides. *Mar. Drugs* **2021**, *19*, 661. [CrossRef] [PubMed]

97. Shiraki, K.; Daikoku, T. Favipiravir, an anti-influenza drug against life-threatening RNA virus infections. *Pharmacol. Ther.* **2020**, *209*, 107512. [CrossRef]

98. Łagocka, R.; Dziedziejko, V.; Kłos, P.; Pawlik, A. Favipiravir in Therapy of Viral Infections. *J. Clin. Med.* **2021**, *10*, 273. [CrossRef]

99. Bixler, S.L.; Bocan, T.M.; Wells, J.; Wetzel, K.S.; Van Tongeren, S.A.; Dong, L.; Garza, N.L.; Donnelly, G.; Cazares, L.H.; Nuss, J.; et al. Efficacy of favipiravir (T-705) in nonhuman primates infected with Ebola virus or Marburg virus. *Antivir. Res.* **2018**, *151*, 97–104. [CrossRef]

100. Cheng, S.; Wang, Y.; Zhang, Z.; Lv, X.; Gao, G.F.; Shao, Y.; Ma, L.; Li, X. Enfuvirtide−PEG conjugate: A potent HIV fusion inhibitor with improved pharmacokinetic properties. *Eur. J. Med. Chem.* **2016**, *121*, 232–237. [CrossRef]

101. A Cooper, D.; Lange, J.M. Peptide inhibitors of virus—cell fusion: Enfuvirtide as a case study in clinical discovery and development. *Lancet Infect. Dis.* **2004**, *4*, 426–436. [CrossRef]

102. Wolf, M.C.; Freiberg, A.N.; Zhang, T.; Akyol-Ataman, Z.; Grock, A.; Hong, P.W.; Li, J.; Watson, N.F.; Fang, A.Q.; Aguilar, H.C.; et al. A broad-spectrum antiviral targeting entry of enveloped viruses. *Proc. Natl. Acad. Sci. USA* **2010**, *107*, 3157–3162. [CrossRef]

103. Vernet, M.-A.; Reynard, S.; Fizet, A.; Schaeffer, J.; Pannetier, D.; Guedj, J.; Rives, M.; Georges, N.; Garcia-Bonnet, N.; Sylla, A.I.; et al. Clinical, virological, and biological parameters associated with outcomes of Ebola virus infection in Macenta, Guinea. *J. Clin. Investig.* **2017**, *2*, e88864. [CrossRef] [PubMed]

104. Martines, R.B.; Ng, D.; Greer, P.W.; Rollin, P.; Zaki, S.R. Tissue and cellular tropism, pathology and pathogenesis of Ebola and Marburg viruses. *J. Pathol.* **2014**, *235*, 153–174. [CrossRef] [PubMed]

105. Scoon, W.A.; Mancio-Silva, L.; Suder, E.L.; Villacorta-Martin, C.; Lindstrom-Vautrin, J.; Bernbaum, J.G.; Mazur, S.; Johnson, R.F.; Olejnik, J.; Flores, E.Y.; et al. Ebola virus infection induces a delayed type I IFN response in bystander cells and the shutdown of key liver genes in human iPSC-derived hepatocytes. *Stem Cell Rep.* **2022**, *17*, 2286–2302. [CrossRef] [PubMed]

106. Wishart, D.S.; Feunang, Y.D.; Guo, A.C.; Lo, E.J.; Marcu, A.; Grant, J.R.; Sajed, T.; Johnson, D.; Li, C.; Sayeeda, Z.; et al. DrugBank 5.0: A Major Update to the DrugBank Database for 2018. *Nucleic Acids Res.* **2018**, *46*, D1074–D1082. [CrossRef] [PubMed]

107. Wishart, D.S.; Knox, C.; Guo, A.C.; Cheng, D.; Shrivastava, S.; Tzur, D.; Gautam, B.; Hassanali, M. DrugBank: A knowledgebase for drugs, drug actions and drug targets. *Nucleic Acids Res.* **2008**, *36*, D901–D906. [CrossRef] [PubMed]

108. Kachur, K.; Suntres, Z.E. The antimicrobial properties of ginseng and ginseng extracts. *Expert Rev. Anti-Infect. Ther.* **2015**, *14*, 81–94. [CrossRef]

109. Im, K.; Kim, J.; Min, H. Ginseng, the natural effectual antiviral: Protective effects of Korean Red Ginseng against viral infection. *J. Ginseng Res.* **2016**, *40*, 309–314. [CrossRef]

110. Yoo, Y.C.; Lee, J.; Park, S.R.; Nam, K.Y.; Cho, Y.H.; Choi, J.E. Protective effect of ginsenoside-Rb2 from Korean red ginseng on the lethal infection of haemagglutinating virus of Japan in mice. *J. Ginseng Res.* **2013**, *37*, 80–86. [CrossRef]

111. Tan, B.; Giangaspero, M.; Sun, N.; Jin, Y.; Liu, K.; Wang, Q.; Cheng, S.; Wang, Y.; Zhang, S. Antiviral Effect of Ginsenoside Rb2 and Rb3 Against Bovine Viral Diarrhea Virus and Classical Swine Fever Virus in vitro. *Front. Vet. Sci.* **2021**, *8*, 1413. [CrossRef]

112. Dong, W.; Farooqui, A.; Leon, A.J.; Kelvin, D.J. Inhibition of influenza A virus infection by ginsenosides. *PLoS ONE* **2017**, *12*, e0171936. [CrossRef]

113. Chen, C.; Shen, J.-L.; Liang, C.-S.; Sun, Z.-C.; Jiang, H.-F. First Discovery of Beta-Sitosterol as a Novel Antiviral Agent against White Spot Syndrome Virus. *Int. J. Mol. Sci.* **2022**, *23*, 10448. [CrossRef] [PubMed]

114. Ortiz-López, T.; Borges-Argáez, R.; Ayora-Talavera, G.; Canto-Ramírez, E.; Cetina-Montejo, L.; May-May, A.; Escalante-Erosa, F.; Cáceres-Farfán, M. Bioassay-Guided Fractionation of *Erythrostemon yucatanensis* (Greenm.) Gagnon & GP Lewis Components with Anti-hemagglutinin Binding Activity against Influenza A/H1N1 Virus. *Molecules* **2022**, *27*, 5494. [CrossRef]

115. Kazakova, O.B.; Giniyatullina, G.V.; Yamansarov, E.Y.; Tolstikov, G.A. Betulin and ursolic acid synthetic derivatives as inhibitors of Papilloma virus. *Bioorganic Med. Chem. Lett.* **2010**, *20*, 4088–4090. [CrossRef]

116. Li, B.-Y.; Hu, Y.; Li, J.; Shi, K.; Shen, Y.-F.; Zhu, B.; Wang, G.-X. Ursolic acid from Prunella vulgaris L. efficiently inhibits IHNV infection in vitro and in vivo. *Virus Res.* **2019**, *273*, 197741. [CrossRef] [PubMed]

117. Tohmé, M.; Giménez, M.; Peralta, A.; Colombo, M.; Delgui, L. Ursolic acid: A novel antiviral compound inhibiting rotavirus infection in vitro. *Int. J. Antimicrob. Agents* **2019**, *54*, 601–609. [CrossRef]

118. Kong, L.; Li, S.; Liao, Q.; Zhang, Y.; Sun, R.; Zhu, X.; Zhang, Q.; Wang, J.; Wu, X.; Fang, X.; et al. Oleanolic acid and ursolic acid: Novel hepatitis C virus antivirals that inhibit NS5B activity. *Antivir. Res.* **2013**, *98*, 44–53. [CrossRef] [PubMed]

119. Jaisi, A.; Prema, P.; Madla, S.; Lee, Y.; Septama, A.W.; Morita, H. Investigation of HIV-1 Viral Protein R Inhibitory Activities of Twelve Thai Medicinal Plants and Their Commercially Available Major Constituents. *Chem. Biodivers.* **2021**, *18*, e2100540. [CrossRef] [PubMed]

120. Shi, X.; Yu, L.; Zhang, Y.; Liu, Z.; Zhang, H.; Zhang, Y.; Liu, P.; Du, P. Glycyrrhetinic acid alleviates hepatic inflammation injury in viral hepatitis disease via a HMGB1-TLR4 signaling pathway. *Int. Immunopharmacol.* **2020**, *84*, 106578. [CrossRef]

121. Wang, L.-J.; Geng, C.-A.; Ma, Y.-B.; Huang, X.-Y.; Luo, J.; Chen, H.; Zhang, X.-M.; Chen, J.-J. Synthesis, biological evaluation and structure–activity relationships of glycyrrhetinic acid derivatives as novel anti-hepatitis B virus agents. *Bioorganic Med. Chem. Lett.* **2012**, *22*, 3473–3479. [CrossRef]

122. Yi, Y.; Li, J.; Lai, X.; Zhang, M.; Kuang, Y.; Bao, Y.-O.; Yu, R.; Hong, W.; Muturi, E.; Xue, H.; et al. Natural triterpenoids from licorice potently inhibit SARS-CoV-2 infection. *J. Adv. Res.* **2021**, *36*, 201–210. [CrossRef]

123. Bailly, C.; Vergoten, G. Glycyrrhizin: An alternative drug for the treatment of COVID-19 infection and the associated respiratory syndrome? *Pharmacol. Ther.* **2020**, *214*, 107618. [CrossRef]

124. Elebeedy, D.; Badawy, I.; Elmaaty, A.A.; Saleh, M.M.; Kandeil, A.; Ghanem, A.; Kutkat, O.; Alnajjar, R.; El Maksoud, A.I.A.; Al-Karmalawy, A.A. In vitro and computational insights revealing the potential inhibitory effect of Tanshinone IIA against influenza A virus. *Comput. Biol. Med.* **2021**, *141*, 105149. [CrossRef] [PubMed]

125. Lin, J.-C.; Cherng, J.-M.; Hung, M.-S.; Baltina, L.A.; Baltina, L.; Kondratenko, R. Inhibitory effects of some derivatives of glycyrrhizic acid against Epstein-Barr virus infection: Structure–activity relationships. *Antivir. Res.* **2008**, *79*, 6–11. [CrossRef] [PubMed]

126. Loe, M.W.C.; Hao, E.; Chen, M.; Li, C.; Lee, R.C.H.; Zhu, I.X.Y.; Teo, Z.Y.; Chin, W.-X.; Hou, X.; Deng, J.; et al. Betulinic acid exhibits antiviral effects against dengue virus infection. *Antivir. Res.* **2020**, *184*, 104954. [CrossRef] [PubMed]

127. Hong, E.-H.; Song, J.H.; Bin Kang, K.; Sung, S.H.; Ko, H.-J.; Yang, H. Anti-Influenza Activity of Betulinic Acid from Zizyphus jujuba on Influenza A/PR/8 Virus. *Biomol. Ther.* **2015**, *23*, 345–349. [CrossRef]

128. Alhadrami, H.; Sayed, A.; Sharif, A.; Azhar, E.; Rateb, M. Olive-Derived Triterpenes Suppress SARS CoV-2 Main Protease: A Promising Scaffold for Future Therapeutics. *Molecules* **2021**, *26*, 2654. [CrossRef]

129. Yao, D.; Li, H.; Gou, Y.; Zhang, H.; Vlessidis, A.G.; Zhou, H.; Evmiridis, N.P.; Liu, Z. Betulinic acid-mediated inhibitory effect on hepatitis B virus by suppression of manganese superoxide dismutase expression. *FEBS J.* **2009**, *276*, 2599–2614. [CrossRef] [PubMed]

130. Lin, C.-K.; Tseng, C.-K.; Chen, K.-H.; Wu, S.-H.; Liaw, C.-C.; Lee, J.-C. Betulinic acid exerts anti-hepatitis C virus activity via the suppression of NF-κB- and MAPK-ERK1/2-mediated CO_{X-2} expression. *Br. J. Pharmacol.* **2015**, *172*, 4481–4492. [CrossRef]

131. Bellampalli, S.S.; Ji, Y.; Moutal, A.; Cai, S.; Wijeratne, E.K.; Gandini, M.A.; Yu, J.; Chefdeville, A.; Dorame, A.; Chew, L.A.; et al. Betulinic acid, derived from the desert lavender Hyptis emoryi, attenuates paclitaxel-, HIV-, and nerve injury–associated peripheral sensory neuropathy via block of N- and T-type calcium channels. *Pain* **2018**, *160*, 117–135. [CrossRef] [PubMed]

132. Theo, A.; Masebe, T.; Suzuki, Y.; Kikuchi, H.; Wada, S.; Obi, C.L.; Bessong, P.O.; Usuzawa, M.; Oshima, Y.; Hattori, T. Peltophorum Africanum, a Traditional South African Medicinal Plant, Contains an Anti HIV-1 Constituent, Betulinic Acid. *Tohoku J. Exp. Med.* **2009**, *217*, 93–99. [CrossRef] [PubMed]

133. Navid, M.H.; Laszczyk-Lauer, M.; Reichling, J.; Schnitzler, P. Pentacyclic triterpenes in birch bark extract inhibit early step of herpes simplex virus type 1 replication. *Phytomedicine* **2014**, *21*, 1273–1280. [CrossRef]

134. Hu, A.; Li, J.; Tang, W.; Liu, G.; Zhang, H.; Liu, C.; Chen, X. Anthralin Suppresses the Proliferation of Influenza Virus by Inhibiting the Cap-Binding and Endonuclease Activity of Viral RNA Polymerase. *Front. Microbiol.* **2020**, *11*, 178. [CrossRef]

135. Richard, K.; Schonhofer, C.; Giron, L.B.; Rivera-Ortiz, J.; Read, S.; Kannan, T.; Kinloch, N.N.; Shahid, A.; Feilcke, R.; Wappler, S.; et al. The African natural product knipholone anthrone and its analogue anthralin (dithranol) enhance HIV-1 latency reversal. *J. Biol. Chem.* **2020**, *295*, 14084–14099. [CrossRef] [PubMed]

136. Batista, M.N.; Braga, A.C.S.; Campos, G.R.F.; Souza, M.M.; de Matos, R.P.A.; Lopes, T.Z.; Candido, N.M.; Lima, M.L.D.; Machado, F.C.; de Andrade, S.T.Q.; et al. Natural Products Isolated from Oriental Medicinal Herbs Inactivate Zika Virus. *Viruses* **2019**, *11*, 49. [CrossRef] [PubMed]

137. Bei, Y.; Tia, B.; Li, Y.; Guo, Y.; Deng, S.; Huang, R.; Zeng, H.; Li, R.; Wang, G.-F.; Dai, J. Anti-influenza A Virus Effects and Mechanisms of Emodin and Its Analogs via Regulating PPARα/γ-AMPK-SIRT1 Pathway and Fatty Acid Metabolism. *BioMed Res. Int.* **2021**, *2021*, 9066938. [CrossRef]

138. Lin, C.-J.; Lin, H.-J.; Chen, T.-H.; Hsu, Y.-A.; Liu, C.-S.; Hwang, G.-Y.; Wan, L. Polygonum cuspidatum and Its Active Components Inhibit Replication of the Influenza Virus through Toll-Like Receptor 9-Induced Interferon Beta Expression. *PLoS ONE* **2015**, *10*, e0117602. [CrossRef]

139. Dai, J.-P.; Wang, Q.-W.; Su, Y.; Gu, L.-M.; Zhao, Y.; Chen, X.-X.; Chen, C.; Li, W.-Z.; Wang, G.-F.; Li, K.-S. Emodin Inhibition of Influenza A Virus Replication and Influenza Viral Pneumonia via the Nrf2, TLR4, p38/JNK and NF-kappaB Pathways. *Molecules* **2017**, *22*, 1754. [CrossRef] [PubMed]

140. Alam, Z.; Al-Mahdi, Z.; Zhu, Y.; McKee, Z.; Parris, D.S.; Parikh, H.I.; Kellogg, G.E.; Kuchta, A.; McVoy, M.A. Anti-cytomegalovirus activity of the anthraquinone atanyl blue PRL. *Antivir. Res.* **2015**, *114*, 86–95. [CrossRef]

141. Dang, S.-S.; Jia, X.-L.; Song, P.; Cheng, Y.-A.; Zhang, X.; Sun, M.-Z.; Liu, E.-Q. Inhibitory effect of emodin and Astragalus polysaccharideon the replication of HBV. *World J. Gastroenterol.* **2009**, *15*, 5669–5673. [CrossRef]

142. Anantpadma, M.; Lane, T.; Zorn, K.M.; Lingerfelt, M.A.; Clark, A.M.; Freundlich, J.S.; Davey, R.; Madrid, P.B.; Ekins, S. Ebola Virus Bayesian Machine Learning Models Enable New in Vitro Leads. *ACS Omega* **2019**, *4*, 2353–2361. [CrossRef]

143. Zhao, Z.; Martin, C.; Fan, R.; Bourne, P.E.; Xie, L. Drug repurposing to target Ebola virus replication and virulence using structural systems pharmacology. *BMC Bioinform.* **2016**, *17*, 90. [CrossRef] [PubMed]

144. Wang, J.; Li, G.-L.; Ming, S.-L.; Wang, C.-F.; Shi, L.-J.; Su, B.-Q.; Wu, H.-T.; Zeng, L.; Han, Y.-Q.; Liu, Z.-H.; et al. BRD4 inhibition exerts anti-viral activity through DNA damage-dependent innate immune responses. *PLoS Pathog.* **2020**, *16*, e1008429. [CrossRef] [PubMed]

145. Coelho, C.; Gallo, G.; Hardy, L.; Bottazzi, M.E.; Campos, C.; Würtele, M. Biochemical Screening of Potent Zika Virus Protease Inhibitors. *Chemmedchem* **2022**, *17*, e202100695. [CrossRef]

146. Esposito, F.; Carli, I.; Del Vecchio, C.; Xu, L.; Corona, A.; Grandi, N.; Piano, D.; Maccioni, E.; Distinto, S.; Parolin, C.; et al. Sennoside A, derived from the traditional chinese medicine plant Rheum L., is a new dual HIV-1 inhibitor effective on HIV-1 replication. *Phytomedicine* **2016**, *23*, 1383–1391. [CrossRef] [PubMed]

147. Nesměrák, K.; Kudláček, K.; Čambal, P.; Štícha, M.; Kozlik, P.; Červený, V. Authentication of senna extract from the eighteenth century and study of its composition by HPLC–MS. *Mon. Chem. -Chem. Mon.* **2020**, *151*, 1241–1248. [CrossRef]

148. Cheung, Y.Y.; Chen, K.C.; Chen, H.; Seng, E.K.; Chu, J.J.H. Antiviral activity of lanatoside C against dengue virus infection. *Antivir. Res.* **2014**, *111*, 93–99. [CrossRef]

149. Miao, M.; Jing, X.; De Clercq, E.; Li, G. Danoprevir for the Treatment of Hepatitis C Virus Infection: Design, Development, and Place in Therapy. *Drug Des. Dev. Ther.* **2020**, *ume14*, 2759–2774. [CrossRef]

150. Rong, L.; Guedj, J.; Dahari, H.; Coffield, D.J., Jr.; Levi, M.; Smith, P.; Perelson, A.S. Analysis of Hepatitis C Virus Decline during Treatment with the Protease Inhibitor Danoprevir Using a Multiscale Model. *PLoS Comput. Biol.* **2013**, *9*, e1002959. [CrossRef]

151. Jiang, Y.; Andrews, S.W.; Condroski, K.R.; Buckman, B.; Serebryany, V.; Wenglowsky, S.; Kennedy, A.L.; Madduru, M.R.; Wang, B.; Lyon, M.; et al. Discovery of Danoprevir (ITMN-191/R7227), a Highly Selective and Potent Inhibitor of Hepatitis C Virus (HCV) NS3/4A Protease. *J. Med. Chem.* **2013**, *57*, 1753–1769. [CrossRef]

152. Elbedewy, T.A.; Elsebaey, M.A.; Elshweikh, S.A.; Elashry, H.; Abd-Elsalam, S. Predictors for eltrombopag response in patients with hepatitis C virus-associated thrombocytopenia. *Ther. Clin. Risk Manag.* **2019**, *ume15*, 269–274. [CrossRef]

153. Danish, F.-I.; Yasmin, S. The role of eltrombopag in the management of hepatitis C virus-related thrombocytopenia. *Hepatic Med. Evid. Res.* **2013**, *5*, 17–30. [CrossRef] [PubMed]

154. Hunt, L.; Gupta-Wright, A.; Simms, V.; Tamba, F.; Knott, V.; Tamba, K.; Heisenberg-Mansaray, S.; Tamba, E.; Sheriff, A.; Conteh, S.; et al. Clinical presentation, biochemical, and haematological parameters and their association with outcome in patients with Ebola virus disease: An observational cohort study. *Lancet Infect. Dis.* **2015**, *15*, 1292–1299. [CrossRef]

155. Tapia, M.D.; Sow, S.O.; Mbaye, K.D.; Thiongane, A.; Ndiaye, B.P.; Ndour, C.T.; Mboup, S.; Keshinro, B.; Kinge, T.N.; Vernet, G.; et al. Safety, reactogenicity, and immunogenicity of a chimpanzee adenovirus vectored Ebola vaccine in children in Africa: A randomised, observer-blind, placebo-controlled, phase 2 trial. *Lancet Infect. Dis.* **2020**, *20*, 719–730. [CrossRef]

156. Matsumoto, Y.; Matsuura, T.; Aoyagi, H.; Matsuda, M.; Hmwe, S.S.; Date, T.; Watanabe, N.; Watashi, K.; Suzuki, R.; Ichinose, S.; et al. Antiviral Activity of Glycyrrhizin against Hepatitis C Virus In Vitro. *PLoS ONE* **2013**, *8*, e68992. [CrossRef] [PubMed]

157. Michaelis, M.; Geiler, J.; Naczk, P.; Sithisarn, P.; Ogbomo, H.; Altenbrandt, B.; Leutz, A.; Doerr, H.W.; Cinatl, J., Jr. Glycyrrhizin inhibits highly pathogenic H5N1 influenza A virus-induced pro-inflammatory cytokine and chemokine expression in human macrophages. *Med. Microbiol. Immunol.* **2010**, *199*, 291–297. [CrossRef]

158. Wolkerstorfer, A.; Kurz, H.; Bachhofner, N.; Szolar, O.H. Glycyrrhizin inhibits influenza A virus uptake into the cell. *Antivir. Res.* **2009**, *83*, 171–178. [CrossRef] [PubMed]

159. Cinatl, J.; Morgenstern, B.; Bauer, G.; Chandra, P.; Rabenau, H.; Doerr, H. Glycyrrhizin, an active component of liquorice roots, and replication of SARS-associated coronavirus. *Lancet* **2003**, *361*, 2045–2046. [CrossRef]

160. Sakai-Sugino, K.; Uematsu, J.; Kamada, M.; Taniguchi, H.; Suzuki, S.; Yoshimi, Y.; Kihira, S.; Yamamoto, H.; Kawano, M.; Tsurudome, M.; et al. Glycyrrhizin inhibits human parainfluenza virus type 2 replication by the inhibition of genome RNA, mRNA and protein syntheses. *Drug Discov. Ther.* **2017**, *11*, 246–252. [CrossRef] [PubMed]

161. Singh, W.; Karabencheva-Christova, T.G.; Black, G.W.; Ainsley, J.; Dover, L.; Christov, C.Z. Conformational Dynamics, Ligand Binding and Effects of Mutations in NirE an S-Adenosyl-L-Methionine Dependent Methyltransferase. *Sci. Rep.* **2016**, *6*, 20107. [CrossRef]

162. Lobanov, M.Y.; Bogatyreva, N.S.; Galzitskaya, O.V. Radius of gyration as an indicator of protein structure compactness. *Mol. Biol.* **2008**, *42*, 623–628. [CrossRef]

163. Wen, C.-C.; Kuo, Y.-H.; Jan, J.-T.; Liang, P.-H.; Wang, S.-Y.; Liu, H.-G.; Lee, C.-K.; Chang, S.-T.; Kuo, C.-J.; Lee, S.-S.; et al. Specific Plant Terpenoids and Lignoids Possess Potent Antiviral Activities against Severe Acute Respiratory Syndrome Coronavirus. *J. Med. Chem.* **2007**, *50*, 4087–4095. [CrossRef] [PubMed]

164. Kumari, R.; Kumar, R.; Lynn, A. g_mmpbsa—A GROMACS tool for high-throughput MM-PBSA calculations. *J. Chem. Inf. Model.* **2014**, *54*, 1951–1962. [CrossRef]

165. Poli, G.; Granchi, C.; Rizzolio, F.; Tuccinardi, T. Application of MM-PBSA Methods in Virtual Screening. *Molecules* **2020**, *25*, 1971. [CrossRef] [PubMed]

166. Chaudhary, N.; Aparoy, P. Application of per-residue energy decomposition to identify the set of amino acids critical for in silico prediction of CO_{X-2} inhibitory activity. *Heliyon* **2020**, *6*, e04944. [CrossRef]

167. Kwofie, S.K.; Dankwa, B.; Enninful, K.S.; Adobor, C.; Broni, E.; Ntiamoah, A.; Wilson, M.D. Molecular Docking and Dynamics Simulation Studies Predict Munc18b as a Target of Mycolactone: A Plausible Mechanism for Granule Exocytosis Impairment in Buruli Ulcer Pathogenesis. *Toxins* **2019**, *11*, 181. [CrossRef] [PubMed]

168. Wade, A.D.; Huggins, D.J. Optimization of Protein–Ligand Electrostatic Interactions Using an Alchemical Free-Energy Method. *J. Chem. Theory Comput.* **2019**, *15*, 6504–6512. [CrossRef]

169. Sims, P.A.; Wong, C.F.; McCammon, J.A. Charge optimization of the interface between protein kinases and their ligands. *J. Comput. Chem.* **2004**, *25*, 1416–1429. [CrossRef]

170. Sulea, T.; Purisima, E.O. Optimizing Ligand Charges for Maximum Binding Affinity. A Solvated Interaction Energy Approach. *J. Phys. Chem. B* **2001**, *105*, 889–899. [CrossRef]

171. Sterling, T.; Irwin, J.J. ZINC 15—Ligand Discovery for Everyone. *J. Chem. Inf. Model.* **2015**, *55*, 2324–2337. [CrossRef]

172. Kim, S.; Chen, J.; Cheng, T.; Gindulyte, A.; He, J.; He, S.; Li, Q.; Shoemaker, B.A.; Thiessen, P.A.; Yu, B.; et al. PubChem in 2021: New data content and improved web interfaces. *Nucleic Acids Res.* **2021**, *49*, D1388–D1395. [CrossRef]

173. Kim, S.; Thiessen, P.A.; Bolton, E.E.; Chen, J.; Fu, G.; Gindulyte, A.; Han, L.; He, J.; He, S.; Shoemaker, B.A.; et al. PubChem substance and compound databases. *Nucleic Acids Res.* **2016**, *44*, D1202–D1213. [CrossRef] [PubMed]

174. Mendez, D.; Gaulton, A.; Bento, A.P.; Chambers, J.; de Veij, M.; Félix, E.; Magariños, M.P.; Mosquera, J.F.; Mutowo, P.; Nowotka, M.; et al. ChEMBL: Towards direct deposition of bioassay data. *Nucleic Acids Res.* **2019**, *47*, D930–D940. [CrossRef]

175. Gaulton, A.; Bellis, L.J.; Bento, A.P.; Chambers, J.; Davies, M.; Hersey, A.; Light, Y.; McGlinchey, S.; Michalovich, D.; Al-Lazikani, B.; et al. ChEMBL: A large-scale bioactivity database for drug discovery. *Nucleic Acids Res.* **2012**, *40*, D1100–D1107. [CrossRef]

176. Bento, A.P.; Gaulton, A.; Hersey, A.; Bellis, L.J.; Chambers, J.; Davies, M.; Krüger, F.A.; Light, Y.; Mak, L.; McGlinchey, S.; et al. The ChEMBL bioactivity database: An update. *Nucleic Acids Res.* **2013**, *42*, D1083–D1090. [CrossRef] [PubMed]

177. Rutz, A.; Sorokina, M.; Galgonek, J.; Mietchen, D.; Willighagen, E.; Gaudry, A.; Graham, J.G.; Stephan, R.; Page, R.; Vondrášek, J.; et al. The LOTUS initiative for knowledge sharing in Natural Products research. In Proceedings of the GA–69th Annual Meeting 2021, Virtual Conference, Bonn, Germany, 5–8 September 2021.

178. Mohanraj, K.; Karthikeyan, B.S.; Vivek-Ananth, R.P.; Chand, R.P.B.; Aparna, S.R.; Mangalapandi, P.; Samal, A. IMPPAT: A curated database of Indian Medicinal Plants, Phytochemistry And Therapeutics. *Sci. Rep.* **2018**, *8*, 4329. [CrossRef] [PubMed]

179. Abdelgaleil, S.A.M.; Nakatani, M. Antifeeding activity of limonoids from Khaya senegalensis (Meliaceae). *J. Appl. Entomol.* **2003**, *127*, 236–239. [CrossRef]

180. Nakatani, M.; Abdelgaleil, S.A.M.; Kurawaki, J.; Okamura, H.; Iwagawa, T.; Doe, M. Antifeedant Rings B and D Opened Limonoids from *Khaya senegalensis*. *J. Nat. Prod.* **2001**, *64*, 1261–1265. [CrossRef]

181. Abdelgaleil, S.A.; Iwagawa, T.; Doe, M.; Nakatani, M. Antifungal limonoids from the fruits of Khaya senegalensis. *Fitoterapia* **2004**, *75*, 566–572. [CrossRef]

182. Thioune, O.; Ahodikpe, D.; Dieng, M.; Diop, A.B.; Ngom, S.; Lo, I. Inflammatory ointment from shea butter and hy-dro-alcoholic extract of Khaya senegalensis barks (Cailcederat). *Dakar Med.* **2000**, *45*, 113–116.

183. Rabadeaux, C.; Vallette, L.; Sirdaarta, J.; Davis, C.; Cock, I.E. An examination of the Antimicrobial and Anticancer Properties of Khaya senegalensis (Desr.) A. Juss. Bark Extracts. *Pharmacogn. J.* **2017**, *9*, 504–518. [CrossRef]

184. Li, B.; Meng, X.J.; Zhu, L.J.; Jiao, X.Y. Preparative Separation and Purification of Lancifodilactone C from Schisandra Chinensis (Turcz.) Baill by High-Speed Counter-Current Chromatography. *Adv. Mater. Res.* **2013**, *634–638*, 1502–1505. [CrossRef]

185. Li, R.-T.; Xiang, W.; Li, S.-H.; Lin, Z.-W.; Sun, H.-D. Lancifodilactones B−E, New Nortriterpenes from *Schisandra lancifolia*. *J. Nat. Prod.* **2003**, *67*, 94–97. [CrossRef] [PubMed]

186. Xiao, W.-L.; Huang, S.-X.; Zhang, L.; Tian, R.-R.; Wu, L.; Li, X.-L.; Pu, J.-X.; Zheng, Y.-T.; Lu, Y.; Li, R.-T.; et al. Nortriterpenoids from *Schisandra lancifolia*. *J. Nat. Prod.* **2006**, *69*, 650–653. [CrossRef] [PubMed]

187. Borkosky, S.; Bardón, A.; Catalán, C.A.; Díaz, J.G.; Herz, W. Diterpenes from Vernonanthura amplexicaulis. *Phytochemistry* **1995**, *40*, 1477–1479. [CrossRef]

188. Catalán, C.A.; De Iglesias, D.I.; Kavka, J.; Sosa, V.E.; Herz, W. Glaucolides and related sesquiterpene lactones from Vernonia chamaedrys. *Phytochemistry* **1988**, *27*, 197–202. [CrossRef]

189. Anjaneyulu, V.; Ravi, K.; Prasad, K.; Connolly, J. Triterpenoids from Mangifera indica. *Phytochemistry* **1989**, *28*, 1471–1477. [CrossRef]

190. van Eijk, J.L.; Radema, M.H. Lupanin alkaloids and other compounds fromcadia purpurea. *Planta Med.* **1975**, *28*, 139–142. [CrossRef]

191. Loggia, R.; Tubaro, A.; Sosa, S.; Becker, H.; Saar, S.; Isaac, O. The Role of Triterpenoids in the Topical Anti-Inflammatory Activity of *Calendula officinalis* Flowers. *Planta Med.* **1994**, *60*, 516–520. [CrossRef]

192. Rangaswami, S.; Rao, E.V. Chemical components of *Plumieria alba* Linn. *Proc. Indian Acad. Sci.—Sect. A* **1960**, *52*, 173–181. [CrossRef]

193. Catalano, S.; Marsili, A.; Morelli, I.; Pistelli, L.; Scartoni, V. Constituents of the Leaves of *Ilex aquifolium* L. *Planta Med.* **1978**, *33*, 416–417. [CrossRef]

194. Yagishita, K.; Nishimura, M. The Chemical Structure of Neoilexonol. *Biosci. Biotechnol. Biochem.* **1961**, *25*, 844–851. [CrossRef]

195. Hui, W.-H.; Li, M.-M.; Luk, K. Triterpenoids and steroids from Rhodomyrtus tomentosa. *Phytochemistry* **1975**, *14*, 833–834. [CrossRef]

196. Van Veen, T. Wikidata. *Inf. Technol. Libr.* **2019**, *38*, 72–81. [CrossRef]

197. Waagmeester, A.; Stupp, G.; Burgstaller-Muehlbacher, S.; Good, B.M.; Griffith, M.; Griffith, O.L.; Hanspers, K.; Hermjakob, H.; Hudson, T.S.; Hybiske, K.; et al. Wikidata as a knowledge graph for the life sciences. *Elife* **2020**, *9*, e52614. [CrossRef] [PubMed]

198. Kalvatchev, Z.; Walder, R.; Garzaro, D. Anti-HIV activity of extracts from Calendula officinalis flowers. *Biomed. Pharmacother.* **1997**, *51*, 176–180. [CrossRef]

199. Rahman, A.U.; Naz, H.; Fadimatou; Makhmoor, T.; Yasin, A.; Fatima, N.; Ngounou, F.N.; Kimbu, S.F.; Sondengam, B.L.; Choudhary, M.I. Bioactive Constituents from *Boswellia papyrifera*. *J. Nat. Prod.* **2005**, *68*, 189–193. [CrossRef]

200. Al-Harrasi, A.; Ali, L.; Ceniviva, E.; Al-Rawahi, A.; Hussain, J.; Hussain, H.; Rehman, N.; Abbas, G. Antiglycation and Antioxidant Activities and HPTLC Analysis of *Boswellia sacra* Oleogum Resin: The Sacred Frankincense. *Trop. J. Pharm. Res.* **2013**, *12*, 597–602. [CrossRef]

201. Al-Yahya, A.A.; Asad, M.; Sadaby, A.; Alhussaini, M.S. Repeat oral dose safety study of standardized methanolic extract of Boswellia sacra oleo gum resin in rats. *Saudi J. Biol. Sci.* **2019**, *27*, 117–123. [CrossRef]

202. Al Amri, I.; Mabood, F.; Kadim, I.T.; Alkindi, A.; Al-Harrasi, A.; Al-Hashmi, S.; Abbas, G.; Hamaed, A.; Ahmed, B.; Al-Shuhaimi, J.; et al. Evaluation of the solubility of 11-keto-β-boswellic acid and its histological effect on the diabetic mice liver using a novel technique. *Vet. World* **2021**, *14*, 1797. [CrossRef]

203. Mehta, M.; Satija, S.; Garg, M. Comparison Between HPLC and HPTLC Densitometry for the Determination of 11-keto-Beta-boswellic acid and 3- acetyl-11-keto-Beta-boswellic acid from Boswellia serrata Extract. *Indian J. Pharm. Educ. Res.* **2016**, *50*, 418–423. [CrossRef]

204. Katragunta, K.; Siva, B.; Kondepudi, N.; Vadaparthi, P.R.; Rao, N.R.; Tiwari, A.K.; Babu, K.S. Estimation of boswellic acids in herbal formulations containing Boswellia serrata extract and comprehensive characterization of secondary metabolites using UPLC-Q-Tof-MSe. *J. Pharm. Anal.* **2019**, *9*, 414–422. [CrossRef] [PubMed]

205. von Rhein, C.; Weidner, T.; Henß, L.; Martin, J.; Weber, C.; Sliva, K.; Schnierle, B.S. Curcumin and Boswellia serrata gum resin extract inhibit chikungunya and vesicular stomatitis virus infections in vitro. *Antivir. Res.* **2016**, *125*, 51–57. [CrossRef] [PubMed]

206. Goswami, D.; Das Mahapatra, A.; Banerjee, S.; Kar, A.; Ojha, D.; Mukherjee, P.K.; Chattopadhyay, D. Boswellia serrata oleo-gum-resin and β-boswellic acid inhibits HSV-1 infection in vitro through modulation of NF-κB and p38 MAP kinase signaling. *Phytomedicine* **2018**, *51*, 94–103. [CrossRef] [PubMed]

207. Siemoneit, U.; Pergola, C.; Jazzar, B.; Northoff, H.; Skarke, C.; Jauch, J.; Werz, O. On the interference of boswellic acids with 5-lipoxygenase: Mechanistic studies in vitro and pharmacological relevance. *Eur. J. Pharmacol.* **2009**, *606*, 246–254. [CrossRef]

208. Ammon, H.P.T. Modulation of the immune system by Boswellia serrata extracts and boswellic acids. *Phytomedicine* **2011**, *17*, 862–867, Erratum in **2011**, *18*, 334. [CrossRef]

209. Ammon, H. Boswellic extracts and 11-keto-ß-boswellic acids prevent type 1 and type 2 diabetes mellitus by suppressing the expression of proinflammatory cytokines. *Phytomedicine* **2019**, *63*, 153002. [CrossRef]

210. Nouveau, L.; Buatois, V.; Cons, L.; Chatel, L.; Pontini, G.; Pleche, N.; Ferlin, W.G. Immunological analysis of the murine anti-CD3-induced cytokine release syndrome model and therapeutic efficacy of anti-cytokine antibodies. *Eur. J. Immunol.* **2021**, *51*, 2074–2085. [CrossRef]

211. Banerjee, G.; Shokeen, K.; Chakraborty, N.; Agarwal, S.; Mitra, A.; Kumar, S.; Banerjee, P. Modulation of immune response in Ebola virus disease. *Curr. Opin. Pharmacol.* **2021**, *60*, 158–167. [CrossRef]

212. Banadyga, L.; Ebihara, H. Epidemiology and Pathogenesis of Filovirus Infections. In *Biology and Pathogenesis of Rhabdo- and Filoviruses*; World Scientific: Singapore, 2015; pp. 453–486, ISBN 9789814635349.

213. Broni, E.; Kwofie, S.K.; Asiedu, S.O.; Miller, W.A.; Wilson, M.D. A Molecular Modeling Approach to Identify Potential Antileishmanial Compounds Against the Cell Division Cycle (cdc)-2-Related Kinase 12 (CRK12) Receptor of *Leishmania donovani*. *Biomolecules* **2021**, *11*, 458. [CrossRef]

214. Gc, J.B.; Johnson, K.A.; Husby, M.L.; Frick, C.T.; Gerstman, B.S.; Stahelin, R.V.; Chapagain, P.P. Interdomain salt-bridges in the Ebola virus protein VP40 and their role in domain association and plasma membrane localization. *Protein Sci.* **2016**, *25*, 1648–1658. [CrossRef]

215. Deshpande, N.; Addess, K.J.; Bluhm, W.F.; Merino-Ott, J.C.; Townsend-Merino, W.; Zhang, Q.; Knezevich, C.; Xie, L.; Chen, L.; Feng, Z.; et al. The RCSB Protein Data Bank: A redesigned query system and relational database based on the mmCIF schema. *Nucleic Acids Res.* **2004**, *33*, D233–D237. [CrossRef] [PubMed]

216. Burley, S.K.; Berman, H.M.; Kleywegt, G.J.; Markley, J.L.; Nakamura, H.; Velankar, S. Protein Data Bank (PDB): The single global macromolecular structure archive. *Protein Crystallogr.* **2017**, *1067*, 627–641.

217. Yuan, S.; Chan, H.S.; Hu, Z. Using PyMOL as a platform for computational drug design. *WIREs Comput. Mol. Sci.* **2017**, *7*, e1298. [CrossRef]

218. Lee, M.-K.; Lee, K.-H.; Yoo, S.-H.; Park, C.-Y. Impact of initial active engagement in self-monitoring with a telemonitoring device on glycemic control among patients with type 2 diabetes. *Sci. Rep.* **2017**, *7*, 3866. [CrossRef]

219. Rother, K. Introduction to PyMOL. *Methods Mol. Biol. Clift. Nj* **2005**, *635*, 0–32. [CrossRef]

220. Yang, J.; Yan, R.; Roy, A.; Xu, D.; Poisson, J.; Zhang, Y. The I-TASSER Suite: Protein structure and function prediction. *Nat. Methods* **2015**, *12*, 7–8. [CrossRef]

221. Eswar, N.; Eramian, D.; Webb, B.; Shen, M.-Y.; Sali, A. Protein Structure Modeling with MODELLER. *Struct. Proteom. High-Throughput Methods* **2008**, *426*, 145–159. [CrossRef]

222. Fiser, A.; Šali, A. Modeller: Generation and Refinement of Homology-Based Protein Structure Models. *Methods Enzymol.* **2003**, *374*, 461–491. [CrossRef]

223. Kuntal, B.K.; Aparoy, P.; Reddanna, P. EasyModeller: A graphical interface to MODELLER. *BMC Res. Notes* **2010**, *3*, 226. [CrossRef]
224. Abraham, M.J.; Murtola, T.; Schulz, R.; Páll, S.; Smith, J.C.; Hess, B.; Lindahl, E. GROMACS: High performance molecular simulations through multi-level parallelism from laptops to supercomputers. *SoftwareX* **2015**, *1*, 19–25. [CrossRef]
225. Van Der Spoel, D.; Lindahl, E.; Hess, B.; Groenhof, G.; Mark, A.E.; Berendsen, H.J.C. GROMACS: Fast, flexible, and free. *J. Comput. Chem.* **2005**, *26*, 1701–1718. [CrossRef] [PubMed]
226. Zoete, V.; Cuendet, M.A.; Grosdidier, A.; Michielin, O. SwissParam: A fast force field generation tool for small organic molecules. *J. Comput. Chem.* **2011**, *32*, 2359–2368. [CrossRef] [PubMed]
227. Brooks, B.R.; Brooks, C.L., III; MacKerell, A.D., Jr.; Nilsson, L.; Petrella, R.J.; Roux, B.; Won, Y.; Archontis, G.; Bartels, C.; Boresch, S.; et al. CHARMM: The biomolecular simulation program. *J. Comput. Chem.* **2009**, *30*, 1545–1614. [CrossRef] [PubMed]
228. Gautam, B. Energy Minimization. In *Homology Molecular Modeling-Perspectives and Applications*; IntechOpen: London, UK, 2021.
229. Tian, W.; Chen, C.; Lei, X.; Zhao, J.; Liang, J. CASTp 3.0: Computed atlas of surface topography of proteins. *Nucleic Acids Res.* **2018**, *46*, W363–W367. [CrossRef]
230. Binkowski, T.A.; Naghibzadeh, S.; Liang, J. CASTp: Computed Atlas of Surface Topography of proteins. *Nucleic Acids Res.* **2003**, *31*, 3352–3355. [CrossRef] [PubMed]
231. Dundas, J.; Ouyang, Z.; Tseng, J.; Binkowski, A.; Turpaz, Y.; Liang, J. CASTp: Computed atlas of surface topography of proteins with structural and topographical mapping of functionally annotated residues. *Nucleic Acids Res.* **2006**, *34*, W116–W118. [CrossRef]
232. Ntie-Kang, F.; Zofou, D.; Babiaka, S.B.; Meudom, R.; Scharfe, M.; Lifongo, L.L.; Mbah, J.A.; Mbaze, L.M.; Sippl, W.; Efange, S.M.N. AfroDb: A Select Highly Potent and Diverse Natural Product Library from African Medicinal Plants. *PLoS ONE* **2013**, *8*, e78085. [CrossRef]
233. Ntie-Kang, F.; Telukunta, K.K.; Döring, K.; Simoben, C.V.; Moumbock, A.F.A.; Malange, Y.I.; Njume, L.E.; Yong, J.N.; Sippl, W.; Günther, S. NANPDB: A Resource for Natural Products from Northern African Sources. *J. Nat. Prod.* **2017**, *80*, 2067–2076. [CrossRef]
234. Chen, C.Y.-C. TCM Database@Taiwan: The World's Largest Traditional Chinese Medicine Database for Drug Screening In Silico. *PLoS ONE* **2011**, *6*, e15939. [CrossRef]
235. Kwofie, S.K.; Broni, E.; Yunus, F.U.; Nsoh, J.; Adoboe, D.; Miller, W.A.; Wilson, M.D. Molecular Docking Simulation Studies Identifies Potential Natural Product Derived-Antiwolbachial Compounds as Filaricides against Onchocerciasis. *Biomedicines* **2021**, *9*, 1682. [CrossRef]
236. Bennett, R.P.; Finch, C.L.; Postnikova, E.N.; Stewart, R.A.; Cai, Y.; Yu, S.; Liang, J.; Dyall, J.; Salter, J.D.; Smith, H.C.; et al. A Novel Ebola Virus VP40 Matrix Protein-Based Screening for Identification of Novel Candidate Medical Countermeasures. *Viruses* **2020**, *13*, 52. [CrossRef] [PubMed]
237. Kouznetsova, J.; Sum, W.; Martínez-Romero, C.; Schimmer, A.; Zheng, W.; García-Sastre, A. Identification of 53 compounds that block Ebola virus-like particle entry via a repurposing screen of approved drugs. *Emerg. Microbes Infect.* **2014**, *3*, e84. [CrossRef] [PubMed]
238. Kim, S. Exploring Chemical Information in PubChem. *Curr. Protoc.* **2021**, *1*, e217. [CrossRef]
239. Kim, S.; Chen, J.; Cheng, T.; Gindulyte, A.; He, J.; He, S.; Li, Q.; Shoemaker, B.A.; Thiessen, P.A.; Yu, B.; et al. PubChem 2019 update: Improved access to chemical data. *Nucleic Acids Res.* **2019**, *47*, D1102–D1109. [CrossRef] [PubMed]
240. Rappe, A.K.; Casewit, C.J.; Colwell, K.S.; Goddard, W.A.; Skiff, W.M. UFF, a full periodic table force field for molecular mechanics and molecular dynamics simulations. *J. Am. Chem. Soc.* **1992**, *114*, 10024–10035. [CrossRef]
241. O'Boyle, N.M.; Banck, M.; James, C.A.; Morley, C.; Vandermeersch, T.; Hutchison, G.R. Open babel: An open chemical toolbox. *J. Cheminform.* **2011**, *3*, 33. [CrossRef]
242. Dallakyan, S.; Olson, A.J. Small-molecule library screening by docking with pyrx. *Methods Mol. Biol.* **2015**, *1263*, 243–250.
243. Mysinger, M.M.; Carchia, M.; Irwin, J.J.; Shoichet, B.K. Directory of Useful Decoys, Enhanced (DUD-E): Better Ligands and Decoys for Better Benchmarking. *J. Med. Chem.* **2012**, *55*, 6582–6594. [CrossRef]
244. Lionta, E.; Spyrou, G.; Vassilatis, D.K.; Cournia, Z. Structure-Based Virtual Screening for Drug Discovery: Principles, Applications and Recent Advances. *Curr. Top. Med. Chem.* **2014**, *14*, 1923–1938. [CrossRef]
245. Cavasotto, C.; Orry, A.J.W. Ligand Docking and Structure-based Virtual Screening in Drug Discovery. *Curr. Top. Med. Chem.* **2007**, *7*, 1006–1014. [CrossRef]
246. Trott, O.; Olson, A.J. AutoDock Vina: Improving the speed and accuracy of docking with a new scoring function, efficient optimization, and multithreading. *J. Comput. Chem.* **2010**, *31*, 455–461. [CrossRef] [PubMed]
247. Breznik, M.; Ge, Y.; Bluck, J.P.; Briem, H.; Hahn, D.F.; Christ, C.D.; Mortier, J.; Mobley, D.L.; Meier, K. Prioritizing Small Sets of Molecules for Synthesis through in-silico Tools: A Comparison of Common Ranking Methods. *Chemmedchem* **2022**, *18*, e202200425. [CrossRef] [PubMed]
248. Warren, G.L.; Andrews, C.W.; Capelli, A.-M.; Clarke, B.; LaLonde, J.; Lambert, M.H.; Lindvall, M.; Nevins, N.; Semus, S.F.; Senger, S.; et al. A Critical Assessment of Docking Programs and Scoring Functions. *J. Med. Chem.* **2005**, *49*, 5912–5931. [CrossRef] [PubMed]
249. Ramírez, D.; Caballero, J. Is It Reliable to Use Common Molecular Docking Methods for Comparing the Binding Affinities of Enantiomer Pairs for Their Protein Target? *Int. J. Mol. Sci.* **2016**, *17*, 525. [CrossRef] [PubMed]

250. Leeson, P.D.; Springthorpe, B. The influence of drug-like concepts on decision-making in medicinal chemistry. *Nat. Rev. Drug Discov.* **2007**, *6*, 881–890. [CrossRef] [PubMed]

251. Daina, A.; Michielin, O.; Zoete, V. SwissADME: A free web tool to evaluate pharmacokinetics, drug-likeness and medicinal chemistry friendliness of small molecules. *Sci. Rep.* **2017**, *7*, 42717. [CrossRef]

252. Dodda, L.; De Vaca, I.C.; Tirado-Rives, J.; Jorgensen, W.L. LigParGen web server: An automatic OPLS-AA parameter generator for organic ligands. *Nucleic Acids Res.* **2017**, *45*, W331–W336. [CrossRef]

253. Lu, C.; Wu, C.; Ghoreishi, D.; Chen, W.; Wang, L.; Damm, W.; Ross, G.A.; Dahlgren, M.K.; Russell, E.; Von Bargen, C.D.; et al. OPLS4: Improving Force Field Accuracy on Challenging Regimes of Chemical Space. *J. Chem. Theory Comput.* **2021**, *17*, 4291–4300. [CrossRef]

254. Robertson, M.J.; Tirado-Rives, J.; Jorgensen, W.L. Improved Peptide and Protein Torsional Energetics with the OPLS-AA Force Field. *J. Chem. Theory Comput.* **2015**, *11*, 3499–3509. [CrossRef]

255. Turner, P. *XMGRACE*, Version 5.1 ed; Center for Coastal and Land-Margin Research, Oregon Graduate Institute of Science and Technology: Beaverton, OR, USA, 2005.

256. Darko, L.K.S.; Broni, E.; Amuzu, D.S.Y.; Wilson, M.D.; Parry, C.S.; Kwofie, S.K. Computational Study on Potential Novel Anti-Ebola Virus Protein VP35 Natural Compounds. *Biomedicines* **2021**, *9*, 1796. [CrossRef]

257. Kwofie, S.K.; Broni, E.; Teye, J.; Quansah, E.; Issah, I.; Wilson, M.D.; Miller, W.A., III; Tiburu, E.K.; Bonney, J.H.K. Pharmacoinformatics-based identification of potential bioactive compounds against Ebola virus protein VP24. *Comput. Biol. Med.* **2019**, *113*, 103414. [CrossRef] [PubMed]

258. Adams, J.; Agyenkwa-Mawuli, K.; Agyapong, O.; Wilson, M.D.; Kwofie, S.K. EBOLApred: A machine learning-based web application for predicting cell entry inhibitors of the Ebola virus. *Comput. Biol. Chem.* **2022**, *101*, 107766. [CrossRef] [PubMed]